Two-bubble class approach based on measured bubble size distribution for bubble columns with and without internals

Möller, F.; Kipping, R.; Lavetty, C.; Hampel, U.; Schubert, M.;

Originally published:

January 2019

Industrial & Engineering Chemistry Research 58(2019)8, 2759-2769

DOI: https://doi.org/10.1021/acs.iecr.8b05784

Two-bubble class approach based on measured bubble size distribution for bubble columns with and without internals

Journal:	*Industrial & Engineering Chemistry Research*
Manuscript ID	Draft
Manuscript Type:	Article
Date Submitted by the Author:	n/a
Complete List of Authors:	Möller, Felix; Helmholtz-Zentrum Dresden-Rossendorf, Institute of Fluid Dynamics Kipping, Ragna; Technische Universitat Dresden, Chair of Imaging Techniques in Energy and Process Engineering Lavetty, Craig; Helmholtz-Zentrum Dresden-Rossendorf, Institute of Fluid Dynamics Hampel, Uwe; Helmholtz-Zentrum Dresden-Rossendorf, Institute of Fluid Dynamics; Technische Universitat Dresden, Chair of Imaging Techniques in Energy and Process Engineering Schubert, Markus; Helmholtz-Zentrum Dresden-Rossendorf, Institute of Fluid Danamics

Two-bubble class approach based on measured bubble size distribution for bubble columns with and without internals

Felix Möller[1,], Ragna Kipping[2], Craig Lavetty[1], Uwe Hampel[1, 2], Markus Schubert[1]*

[1]Institute of Fluid Dynamics, Helmholtz-Zentrum Dresden-Rossendorf, Bautzner Landstr. 400, 01328 Dresden, Germany

[2]Chair of Imaging Techniques in Energy and Process Engineering, Technische Universität Dresden, 01062 Dresden, Germany

[*]Corresponding author

Keywords

Bubble column, heat exchanger internals, two-bubble class approach, bubble size distribution, gas holdup, bubble rise velocity, ultrafast X-ray tomography

Abstract

The complex flow patterns in bubble columns can be phenomenologically described by the two-bubble class approach. For the first time, this approach is applied to bubble columns with dense internals. Internals of square and triangular pitch tube patterns of two tube sizes (8×10^{-3} and 13×10^{-3} m) with flat and U-tube bottom design and cross-sectional occupation of ~25% were inserted in a bubble column of 0.1 m diameter and 2 m height. Contrary to the well-known gas disengagement technique, dual-plane ultrafast X-ray computed tomography data have been used for the bubble class allocation. Experiments were performed at superficial gas velocities ranging from 0.02 m s^{-1} to 0.20 m s^{-1} to cover homogeneous and heterogeneous flow conditions. The contributions of small and large bubble classes on total holdup, flow structure and bubble rise velocities were determined. Furthermore, the regime transition onset was determined based on the two-bubble class approach. Eventually, new correlations for regime transition, small and large bubble rise velocity, large bubble holdup as well as total holdup are proposed based on sub-channel area, sub-channel hydraulic diameter and occlusion area.

1 Introduction

Bubble column reactors (BCRs) are widely encountered in the chemical process industry due to their easy construction and operation without moving parts, low maintenance costs as well as due to their excellent heat and mass transfer characteristics at comparably low energy input[1]. They are applied for various bulk processes, such as Fischer-Tropsch synthesis, methanol synthesis, waste-water treatment, etc. In order to ensure stable and safe reactor operation, high product selectivity and long catalyst life-time, isothermal processing is preferred[2,3]. A successful heat management is achieved using dense internal heat exchanger tube bundles, which offer large specific heat transfer areas[4–6]. Such heat exchanger tube bundles can occupy up to 60 % of the reactor's cross-section and alter the hydrodynamics significantly[7–14]. While coverages below 5 % are still negligible[10,15], internals that cover more than 20 % increase the total gas holdup significantly [4–10,16–25], which is caused by forced bubble breakup. Hence, smaller bubbles and lower bubble rise velocities are direct consequences of the densely packed internals[10,22–27].

Various approaches to describe the hydrodynamics exist for the design and scale-up of BCRs. Wilkinson et al.[28], Krishna and Ellenberger[29] and Grund[30] proposed a phenomenological approach based on the main flow regimes, i.e. homogenous and heterogeneous flow regime[31,32], and their characteristic bubble behavior as illustrated in Figure 1.

The homogeneous flow regime is encountered at low superficial gas velocities (commonly at $u_g < 0.03\,\mathrm{m\,s^{-1}} \ldots 0.05\,\mathrm{m\,s^{-1}}$) and features rather uniformly sized bubbles of small size (see Figure 1, left) depending on the gas distributor[33]. The small bubbles rise uniformly with a flat radial gas velocity profile[34]. Similarly, the radial liquid velocity profile is flat and only minor recirculation is observed. The heterogeneous flow regime occurs at high superficial gas velocities (commonly at $u_g > 0.08\,\mathrm{m\,s^{-1}}$) and is characterized by the formation of large bubbles, e.g. spherical-cap bubbles (see Figure 1, right), and an increased frequency of bubble breakup and coalescence events. Increased turbulence, a wide bubble size distribution (BSD) and a parabolic gas holdup profile are typical features of the heterogeneous flow regime. Small bubbles (also referred to as dense phase) preferably rise in the wall zone, while large bubbles (also referred to as dilute phase) preferably rise in the column center[35], prompting a gross liquid circulation pattern with some small bubbles trapped within liquid eddies[36]. Simplified, the bubbles are assigned to two bubble classes, namely, small and large bubbles[28,29,37–45].

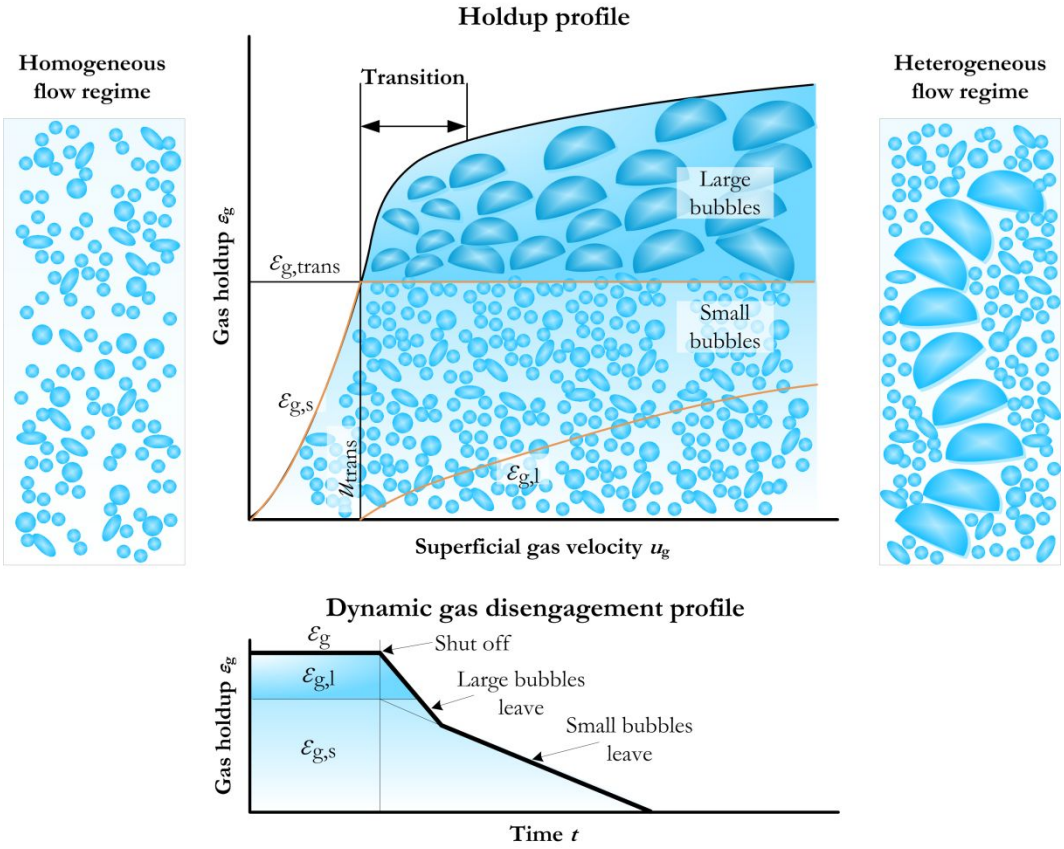

Figure 1: Illustration of TBCA with characteristic flow regimes and gas holdup profile in the upper row and DGD profile below for the determination of regime transition and bubble class holdups according to Grund[30].

Following this two-bubble class approach (TBCA), the formation of large bubbles starts at the onset of the transition between homogeneous and heterogeneous flow (see Figure 1). Accordingly, the following assumptions hold for the gas holdups at the respective regimes:

$$\varepsilon_{g,l} = 0,\ 0 < u_g \leq u_{trans}, \tag{1}$$

$$\varepsilon_{g,l} > 0,\ u_g > u_{trans} \tag{2}$$

and

$$\varepsilon_{g,s} = \varepsilon_{g,trans},\ u_g \geq u_{trans}, \tag{3}$$

where $\varepsilon_{g,l}$, $\varepsilon_{g,s}$ ($\varepsilon_g = \varepsilon_{g,l} + \varepsilon_{g,s}$) and $\varepsilon_{g,trans}$ are large and small bubble class holdups and gas holdup at the transition, respectively, and u_g and u_{trans} represent the superficial gas velocity and the transition velocity. The superficial gas velocities of small and large bubble classes contribute to the total superficial gas velocity according to

$$u_{\mathrm{g}} = u_{\mathrm{g,l}} + u_{\mathrm{g,s}}. \tag{4}$$

Furthermore, the small and large bubble class swarm velocities ($u_{\mathrm{b,s}}$ and $u_{\mathrm{b,l}}$, respectively) are defined as

$$u_{\mathrm{b,l}} = \frac{u_{\mathrm{g,l}}}{\varepsilon_{\mathrm{g,l}}}$$

and

$$u_{\mathrm{b,s}} = \frac{u_{\mathrm{g,s}}}{\varepsilon_{\mathrm{g,s}}}. \tag{5}$$

The total gas holdup can be calculated according to

$$\varepsilon_{\mathrm{g}} = \frac{u_{\mathrm{g}}}{v_{\mathrm{b,s}}}, u_g < u_{\mathrm{trans}}, \tag{6}$$

and

$$\varepsilon_{\mathrm{g}} = \frac{u_{\mathrm{trans}}}{v_{\mathrm{b,s}}} + \frac{u_{\mathrm{g}} - u_{\mathrm{trans}}}{v_{\mathrm{b,l}}}, u_{\mathrm{g}} > u_{\mathrm{trans}}, \tag{7}$$

where $v_{\mathrm{b,s}}$ and $v_{\mathrm{b,l}}$ are the small and large bubble rise velocities.

Commonly, the small and large bubble class holdups are determined by means of the dynamic gas disengagement (DGD) method. Here, the gas supply is abruptly closed. Initially, the fast-rising large bubbles (jointly with small bubbles, which are entrained in the large bubbles' wakes) leave the column followed by the remaining small bubbles. Typically, the gas disengagement is monitored via gas-liquid dispersion height measurements[30,45] or differential pressure measurements[46–48]. The DGD gas holdup profile (see Figure 1) based on the differential pressure measurements is obtained according to

$$\varepsilon_{\mathrm{g}} = \frac{\frac{\Delta P}{\Delta H g} - \rho_{\mathrm{l}}}{\rho_{\mathrm{l}} - \rho_{\mathrm{g}}}, \tag{8}$$

where ρ_{g} and ρ_{l} represent the gas and liquid density, g denotes the earth acceleration and $\Delta P/\Delta H$ is the pressure drop over the measured height confined by the two pressure drop measurement ports.

The disengagement of the two bubble classes is reflected by two distinct slopes of the disengagement profile (see Figure 1), which enables to determine the large and small bubble class holdups graphically. However, it should be mentioned that this technique involves some uncertainties, such as early disengagement of small bubbles caught in the wakes of the large bubbles, late disengagement of small bubbles due to liquid circulation as well as arbitrary graphical separation as discussed by Basha and Morsi[46]. Nevertheless, the DGD method was applied to empty BCRs and several empirical correlations were derived to predict the flow regime transition and to determine gas holdup as well as bubble swarm and rise velocities. Wilkinson et al.[28] proposed correlations for the small bubble class rise velocity, $v_{\mathrm{b,s}}$, and the superficial gas velocity at regime transition, u_{trans}, in bubble columns of different diameters, D, operated with various liquids and gases according to

$$v_{\mathrm{b,s}} = 2.25\frac{\sigma_{\mathrm{l}}}{\eta_{\mathrm{l}}}\left[\frac{{\sigma_{\mathrm{l}}}^3\rho_{\mathrm{l}}}{g\eta_{\mathrm{l}}^4}\right]^{-0.273}\left[\frac{\rho_{\mathrm{l}}}{\rho_{\mathrm{g}}}\right]^{0.03}, \tag{9}$$

and

$$\frac{u_{\mathrm{trans}}}{v_{\mathrm{b,s}}} = \varepsilon_{\mathrm{trans}} = 0.5\exp\left(-193\rho_{\mathrm{g}}^{-0.61}\eta_{\mathrm{l}}^{0.5}\sigma^{0.11}\right). \tag{10}$$

Furthermore, they proposed correlations for the large bubble class rise velocity, $v_{\mathrm{b,l}}$, as well as for small and large bubble class holdups, $\varepsilon_{\mathrm{g,s}}$ and $\varepsilon_{\mathrm{g,l}}$, respectively, for $u_{\mathrm{g}} > u_{\mathrm{trans}}$ according to

$$v_{\mathrm{b,l}} = v_{\mathrm{b,s}} + 2.4\frac{\sigma_{\mathrm{l}}}{\eta_{\mathrm{l}}}\left[\frac{\eta_{\mathrm{l}}(u_{\mathrm{g}} - u_{\mathrm{trans}})}{\sigma_{\mathrm{l}}}\right]^{0.757}\left[\frac{{\sigma_{\mathrm{l}}}^3\rho_l}{g\eta_{\mathrm{l}}^4}\right]\left[\frac{\rho_{\mathrm{l}}}{\rho_{\mathrm{g}}}\right]^{0.077}, \tag{11}$$

$$\varepsilon_{\mathrm{g,l}} = \frac{u_{\mathrm{g}} - u_{\mathrm{trans}}}{v_{\mathrm{b,l}}}, \tag{12}$$

and

$$\varepsilon_{\mathrm{g,s}} = \varepsilon_{\mathrm{trans}}. \tag{13}$$

Krishna and co-workers[29,37] also followed the TBCA and derived a fully empirical and dimensional correlation for the large bubble class holdup, which is

$$\varepsilon_{g,l} = 0.268D^{-0.18}(u_g - u_{b,l})^{0.58}, \quad (14)$$

where $u_{b,l}$ is the superficial gas velocity of the large bubble class. Reilly et al.[49] defined $u_{b,l}$ as the superficial gas velocity at regime transition according to

$$u_{b,l} = u_{trans} = u_{b,s}\varepsilon_{trans}(1 - \varepsilon_{trans}), \quad (15)$$

with

$$u_{b,s} = 0.3521\rho_g^{-0.04}\sigma_l^{0.12}, \quad (16)$$

and

$$\varepsilon_{trans} = 4.457\sqrt{\frac{\rho_g^{0.96}}{\rho_l}\sigma_l^{0.12}}. \quad (17)$$

Beyond these correlations, models were developed dividing the gas phase into large, fast-rising bubbles in the column center, small rising bubbles in the center and recirculating small bubbles in the wall zone. Such TBCA compartment models are utilized to predict the gas phase dynamics and to describe the gas mixing[38–43].

Yet, the aforementioned correlations and models based on the TBCA were developed and validated for empty BCRs only. The effects of internals on the development of the two bubble classes, their contribution to the total gas holdup as well as the bubble rise velocities of the respective bubble classes have not been studied. Thus, this paper aims on assessing the TBCA for BCRs with internals based on experimentally determined bubble characteristics in terms of size as well as class-specific rise velocities and holdups. To cope with the uncertainty of the DGD technique, we employed dual-plane ultrafast X-ray computed tomography (UFXCT) as an alternative and complementing technique to distinguish small and large bubbles based on the determined BSD. The predictive capability of the equations developed by Wilkinson et al.[28] and Krishna and Ellenberger[29] has been tested for BCRs without and with various internals. Eventually, modified correlations are proposed to account for the most relevant geometrical parameters of the internals.

2 Experimental design and measurement methods

2.1 Bubble column setup and operating conditions

The experiments were performed in a cylindrical BCR of 0.1 m inner diameter and 2.0 m total height (Figure 2a). The gas was distributed via a perforated plate with 55 holes of 0.5×10^{-3} m diameter arranged in a triangular pitch (P = 0.01 m) resulting in an open area ratio of 0.14 %. Superficial gas velocities ranging from 0.02 to 0.14 m s^{-1} with increments of 0.02 m s^{-1} were precisely adjusted via two mass flow controllers (Omega, FMA-2608A and FMA-2611A) to cover homogeneous and heterogeneous flow regimes. In addition, experiments at 0.20 m s^{-1} were performed at well-developed heterogeneous flow conditions. For the sake of comparability with the empty column, all superficial gas velocities are based on the free area of the CSA, i.e. area not occupied by the tube bundle. Deionized water and air were used for the experiments and the unaerated liquid height was kept constant at 1.1 m for all experiments.

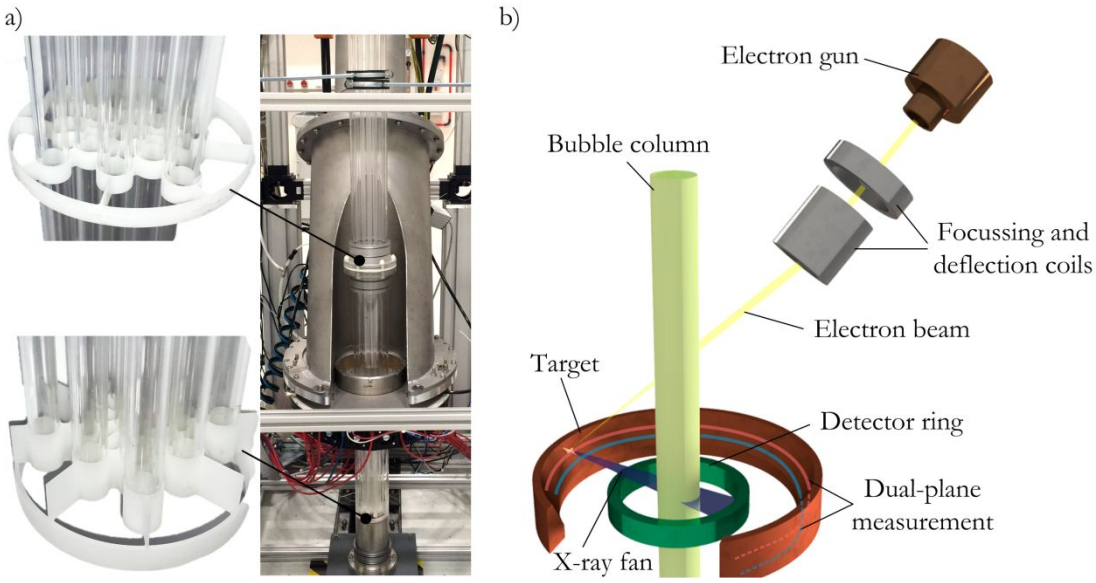

Figure 2: a) Photograph of the setup with images of the 3D-printed spacers and bottom parts as well as b) a schematic and rendered view of the UFXCT facility.

The differential pressure drop for the complementary DGD technique was measured at a temporal resolution of 1,000 Hz with a pressure transducer (PD40, Schneider Messtechnik GmbH) connected with pressure ports located 0.04 m and 0.89 m above the sparger.

2.2 Design of internals

The pitches of the internals were chosen according to the TEMA[50] manufacturing instructions. For an effective heat transfer, the heat exchanger layout guidelines recommend a pitch-to-tube diameter ratio of

approx. 1.3. The number of tubes was chosen to ensure a large surface-to-volume ratio providing a heat removal capacity typical for the Fischer-Tropsch synthesis in BCRs. The area covered by the internals was adjusted at approx. 25 % regardless of tube size and tube pattern. Tubes of 8×10^{-3} m and 13×10^{-3} m outer diameter were arranged in square and triangular pitches. The geometrical details of the internals are summarized in Table 1.

Table 1: Summary of the tube layouts and their specification as well as their geometrical data.

Type	Square 8 (*s8*)	Triangular 8 (*t8*)	Square 13 (*s13*)	Triangular 13 (*t13*)
	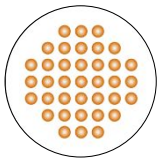	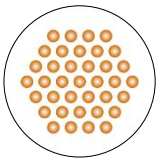	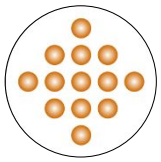	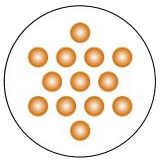
Diameter (d_o) in $\times10^{-3}$m	8.0	8.0	13.0	13.0
Pitch (P) in $\times10^{-3}$m	11.0	11.5	17.5	18.5
Hydraulic diameter (d_h) in $\times10^{-3}$m	7.6	5.6	11.8	8.9
Sub-channel area (A_s) in $\times10^{-6}$m^2	70.7	32.1	173.5	81.8
Coverage (A_c) in %	24	24	23	23
Number of tubes (N)	37	37	13	13

It should be noted that the wall zone (dimensionless radius $r/R \geq 0.75$) was kept free of internals to ensure a better heat removal and an easier maintenance as suggested by others[10,51]. Since a rather narrow BCR was used, the geometrical details were down-scaled from larger columns. As scaling quantities, coverage, pitch-to-tube diameter and ratio of the free wall region were used. The tube bundles were tightly fixed with several 3D-printed spacer grids (see Figure 2a) installed at axial distances of 0.5 m. The distance between the bottom tube ends and the sparger plate was the same as the clearance between wall and bundle. To mimic industrial heat exchangers, a U-tube bottom design was also studied.

2.3 Ultrafast X-ray CT

The UFXCT (Figure 2b) was used to non-invasively visualize the gas phase structure in the cross-section including the sub-channels confined by the tubes at very high temporal resolution for subsequent bubble size analysis and class allocation. Contrary to conventional medical X-ray CT systems, an electron beam is rapidly swept along two circular paths on a tungsten target surrounding the column to create the moving X-ray spot at two heights of 11×10^{-3} m distance. A dual-plane detector ring comprising of 216 detector elements per plane measures the arriving intensities of the X-rays penetrating the BCR. X-ray scanning was performed at a frequency of 1,000 cross-sectional images per second for each plane, i.e. the total

measurement frequency was 2,000 Hz. More information on the principles and technical details of the UFXCT can be found elsewhere[52–58].

3 Post-Processing

3.1 Image-processing

The raw data from the detector readings per beam revolution for each plane are reconstructed via filtered back-projection to obtain the raw image. Subsequently, these data are post-processed to derive phase fraction information (e.g. gas holdup) for every particular position, i.e. image pixel, in the CSA. In the first step, the raw images are normalized between empty as well as liquid-filled BCR, where values between 0 (gas) and 1 (liquid) represent gas-liquid mixtures and values larger than 1 describe the column wall. Then, the empty column reference $(\boldsymbol{\mu_e})$ is subtracted from the normalized data $(\boldsymbol{\mu_n})$ and divided by the difference of liquid filled $(\boldsymbol{\mu_f})$ and empty BCR reference data, according to

$$\boldsymbol{\mu_r} = \frac{\boldsymbol{\mu_n} - \boldsymbol{\mu_e}}{\boldsymbol{\mu_f} - \boldsymbol{\mu_e}} \,. \tag{18}$$

The resulting data matrix for each plane is binarized using a global threshold value (0.65)[59,60]. The matrix has a stack size of 208 × 208 pixels (excluding the pixels outside the CSA and covered by the internal tubes) × 10,000 frames (according to the measurement time of 10 s at a frame rate of 1,000 frames s^{-1}). Eventually, algorithms for the extraction of characteristic hydrodynamic data, such as gas holdup, bubble velocities, gas velocity and BSD are applied as explained below.

3.2 Hydrodynamic data calculation

3.2.1 Total gas holdup

The total gas holdup is calculated based on the averaged gas holdup time series for every pixel of one plane within the CSA according to

$$\varepsilon_{\mathrm{g}} = \frac{\sum_{k=1}^{N_{\mathrm{f}}} \sum_{j=1}^{N_{\mathrm{px}}} \sum_{i=1}^{N_{\mathrm{py}}} \alpha_{\mathrm{i,j,k}}}{N_{\mathrm{f}} \cdot N_{\mathrm{px}} \cdot N_{\mathrm{py}}}, \tag{19}$$

where N_{px} and N_{py} represent the number of valid pixels in the circular cross-section for x and y direction, N_{f} is the number of frames and $\alpha_{\mathrm{i,j,k}}$ describes the local gas holdup.

3.2.2 Bubble size distribution

The BSD is the most important characteristic of the dispersed gas phase to allocate bubbles to small and large bubbles classes, respectively. For the calculation of the BSD, individual bubbles were identified from the binarized 3D data matrix and labeled (see Figure 3). In order to cope with noise and artefacts, bubbles detected in less than three consecutive frames and smaller than four pixels were withdrawn from further analyses[23,25,61].

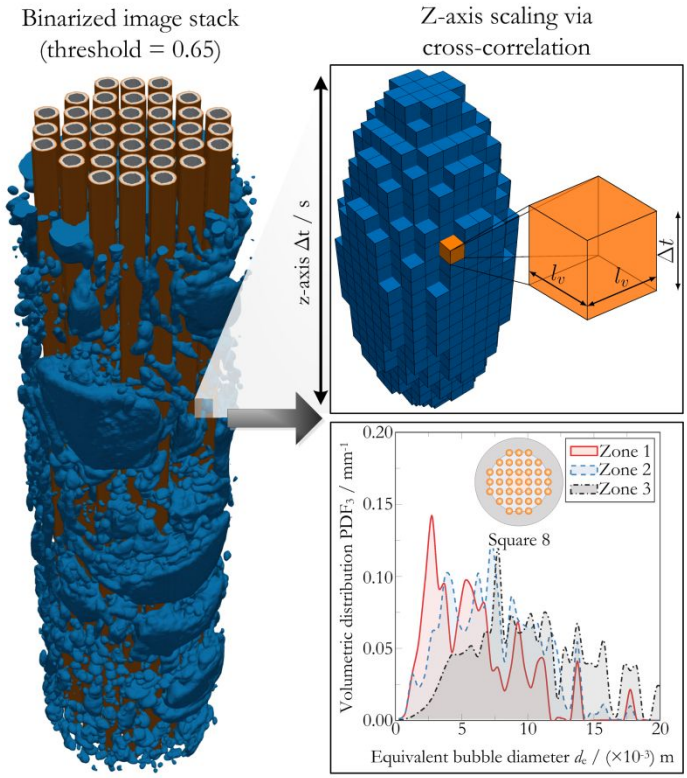

Figure 3: Schematic flow chart for the determination of bubble characteristics from binarized image stacks.

Each bubble features a cluster of n_b voxels. The physical voxel volume is defined as $l_\mathrm{V}^2 \cdot v_\mathrm{b} \cdot \Delta t$, where l_V = 0.5×10^{-3} m is the voxel edge length, $\Delta t =$ 1×10^{-3} s is the time between two subsequent frames (see Figure 3) and v_b is the bubble velocity. By applying cross-correlation algorithms to extract the average bubble velocity, the volume of individual bubbles is calculated as

$$V_\mathrm{b} = n_\mathrm{b} \cdot l_\mathrm{V}^2 \cdot v_\mathrm{b} \cdot \Delta t. \qquad (20)$$

Assuming an approximately spherical bubble shape, the hydraulic diameter can be calculated from the volume of an equivalent sphere as

$$d_{\mathrm{e}} = \left(\frac{6\,V_{\mathrm{b}}}{\pi}\right)^{\frac{1}{3}}. \tag{21}$$

Further details on the post-processing of the UFXCT data for multiphase flows can be found elsewhere[24,58–62].

3.2.3 Bubble rise velocity via bubble pairing

The dual-plane configuration enables the detection of the bubble passage. Several algorithms are available to identify bubbles moving from one plane to the other based on their three-dimensional velocities[63,64]. For a reliable detection of the corresponding bubble pairs, the method of Furuya et al.[64] was applied, which is based on three pre-defined thresholds, namely, a search radius (Δr=11×10^{-3} m), a volume change (Δr_{v}=0.2) and a time lag (Δt). The time lag is a function of the expected bubble velocity and was thus selected depending on the superficial gas velocity. Bubbles fulfilling these criteria are chosen as pairs.

4 Results

4.1 Assessment of classification approaches

In this section, the classification of the small and large bubbles is presented based on the DGD method and the UFXCT technique. Both methods are applied and the bubbles' classification is compared.

4.1.1 Holdup classification via dynamic gas disengagement

Exemplarily, Figure 4 shows the DGD profiles for Square 8 (*s8*) configuration and empty BCR for a superficial gas velocity of 0.20 m s^{-1}, which is in the fully developed heterogeneous flow regime[22,65] featuring small and large bubbles. Upon gas shut-off, mainly the large bubbles leave the reactor followed by the small bubbles. The small bubble class holdup can be determined based on the graphical separation.

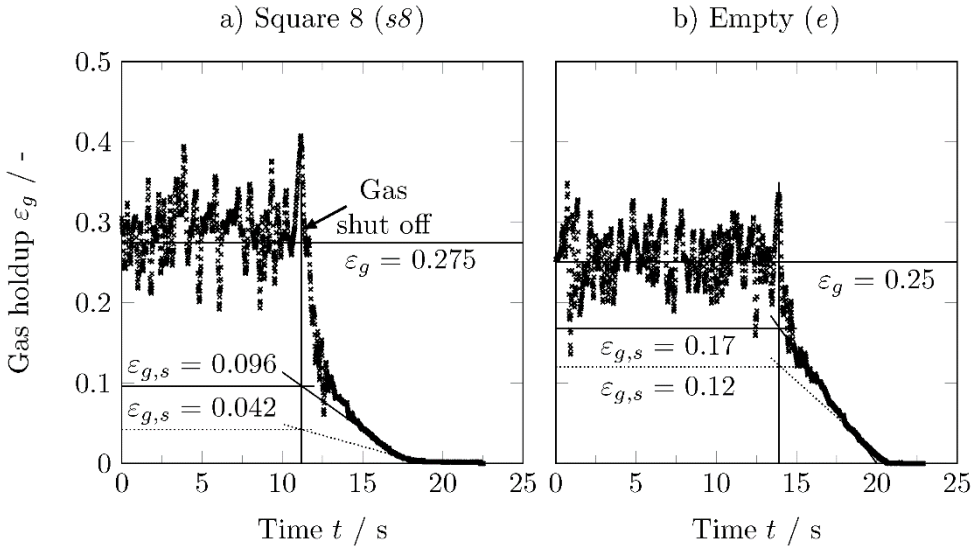

Figure 4: Dynamic gas disengagement profiles for a) Square 8 (*s8*) configuration and b) empty column at superficial gas velocities of 0.20 m s^{-1} (dashed and solid lines represent possible graphical class separation).

Figure 4 illustrates the ambiguous graphical separation of small and large holdup classes (dashed and solid line) as discussed by Basha and Morsi[46]. For example, small bubble class holdups of 0.042 (dashed line) or 0.096 (solid line) can be derived for the Square 8 (*s8*) configuration depending on the respective linear slope. Similar differences are obtained for the empty BCR (Figure 4b) and all other configurations with internals.

4.1.2 Bubble classification via ultrafast X-ray tomography

As an alternative classification approach, BSD data from UFXCT are utilized to distinguish small and large bubbles based on their distribution characteristics. Derived BSD data for same experimental conditions as shown in the previous section (Square 8 (*s8*) configuration and empty bubble column at a superficial gas velocity of 0.20 m s^{-1}) are exemplarily shown in Figure 5.

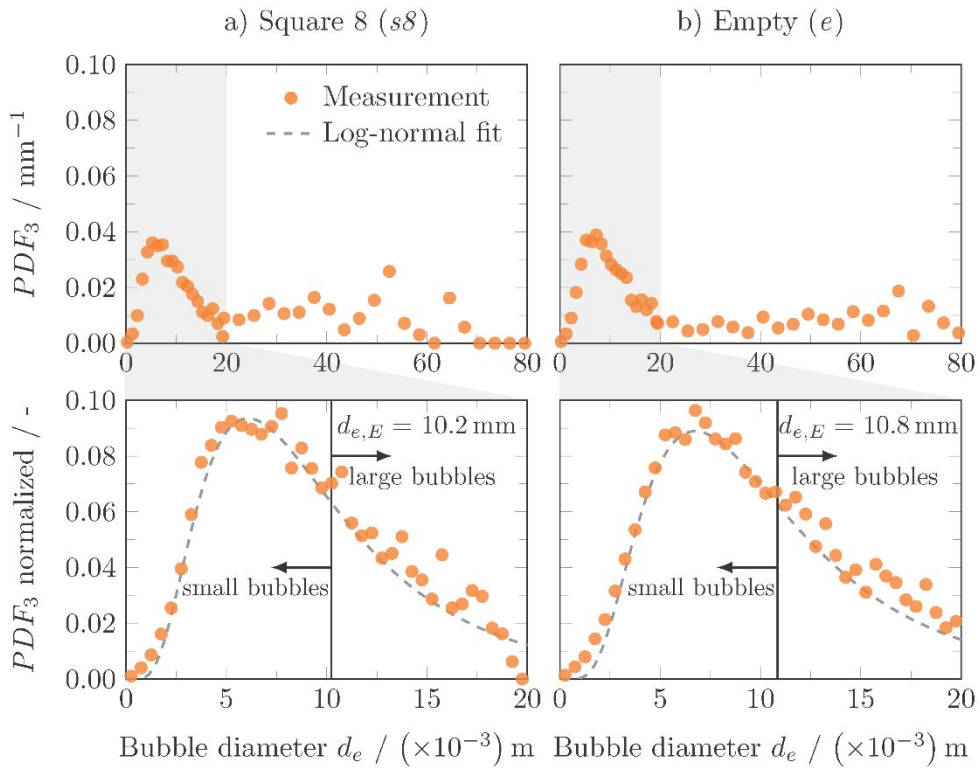

Figure 5: BDS and bubble class allocation at a superficial gas velocity of 0.20 m s^{-1} based on the log-normal distribution for bubbles with equivalent diameter below 0.02 m for a) Square 8 (*s8*) configuration and b) empty bubble column.

The BSDs feature the typical bimodal shape with a distinctive peak for the small bubbles and a widely scattering range for the large bubbles (Figure 5, upper row). The peak of the small bubbles can be described by the log-normal distribution[26,31] according to

$$f(d_e) = \frac{1}{\sigma d_e \sqrt{2\pi}} \exp\left(-\frac{(\ln(d_e) - \mu)^2}{2\sigma^2}\right). \quad (22)$$

Fitting the coefficients σ and μ of Equation 22 for the equivalent diameters up to 0.02 m (Figure 5, lower row), the expectation value $d_{e,E}$ of the small bubble diameter

$$d_{e,E} = \exp\left(\mu + \frac{\sigma^2}{2}\right) \quad (23)$$

can be utilized as the threshold separating small and large bubble classes. The average threshold bubble diameters for all configurations determined at superficial gas velocities from 0.08 m s^{-1} to 0.20 m s^{-1} (representing the heterogeneous flow with bimodal bubble size distributions) are summarized in Table 2.

Following the basic concept of the TBCA, the threshold diameter should be independent from the superficial gas velocity, which is confirmed by the small deviation of the average thresholds. Thus, the classification approach can be considered as very reliable.

Table 2: Average threshold diameter for the small bubble class determined for BCRs with and without internals based on the log-normal distribution.

Configuration	Threshold diameter
Empty (*e*)	$10.8 \pm 0.2 \times 10^{-3}$ m
Square 8 (*s8*)	$10.2 \pm 0.3 \times 10^{-3}$ m
Square u8 (*su8*)	$10.5 \pm 0.3 \times 10^{-3}$ m
Triangular 8 (*t8*)	$10.5 \pm 0.4 \times 10^{-3}$ m
Square 13 (*s13*)	$12.5 \pm 0.4 \times 10^{-3}$ m
Triangular 13 (*t13*)	$12.3 \pm 0.3 \times 10^{-3}$ m

Depending on the configuration, the determined average threshold bubble diameter are in the range from 10×10^{-3} m to 12×10^{-3} m, which agrees fairly well with the definition of Maretto and Krishna[44] and Maretto and Piccolo[66]. The bubbles allocation to the respective classes is visualized as pseudo 3D flow structures (stacked UFXCT images, where vertical axis represents the time) in Figure 6. Here, bubbles color-coded in blue and orange belong to small and large bubble class, respectively.

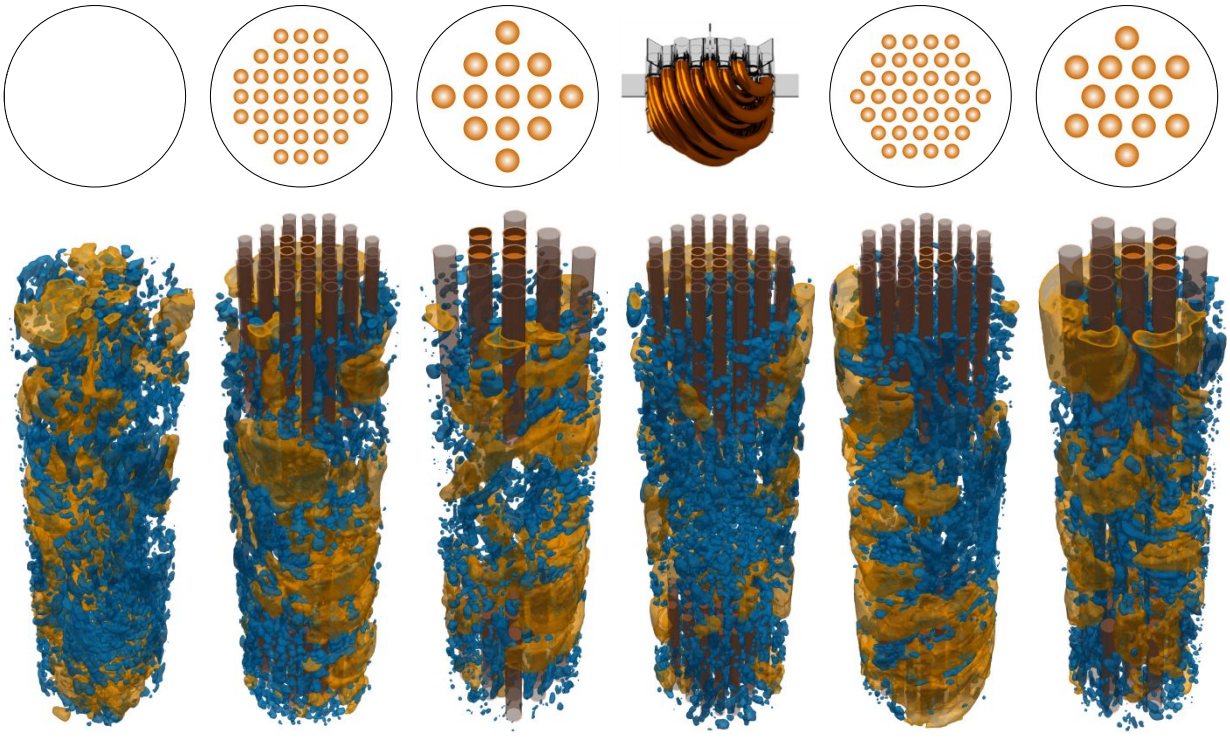

Figure 6: Pseudo 3D flow structures incorporating the distribution of small and large bubbles for a superficial gas velocity of 0.20 m s^{-1}.

The bubble allocation according to their size illustrates the flow structures for the configurations. For the empty BCR, the large bubbles preferably rise within the column's core forming a helical flow structure followed by small bubbles trapped in their wakes, which confirms the flow description by Chen et al.[67] However, if internals are inserted, the flow structure changes and large bubbles rise preferably in the wall region on large helical paths. A larger portion of the small bubbles, in turn, is trapped within the tube bundle. Although the effect of tube pattern and sub-channel size on the flow structure is less distinct, the number of large bubbles is lower for the smaller tubes as already described by our previous study[23].

4.1.3 Comparison of the classification methods

The comparison between the DGD approach and the new proposed method based on the UFXCT data is shown in Figure 7 for empty BCR as well as Square 8 (*s8*) configuration in terms of gas holdups as function of the superficial gas velocity. While total and small bubble class holdup values are directly obtained from the DGD, the respective gas holdups from UFXCT data are determined based on the described bubble size allocation. Data for the empty bubble column (D = 0.1 m) from Grund[30] (obtained with the DGD approach) are also shown in Figure 7 to compare the results with the literature.

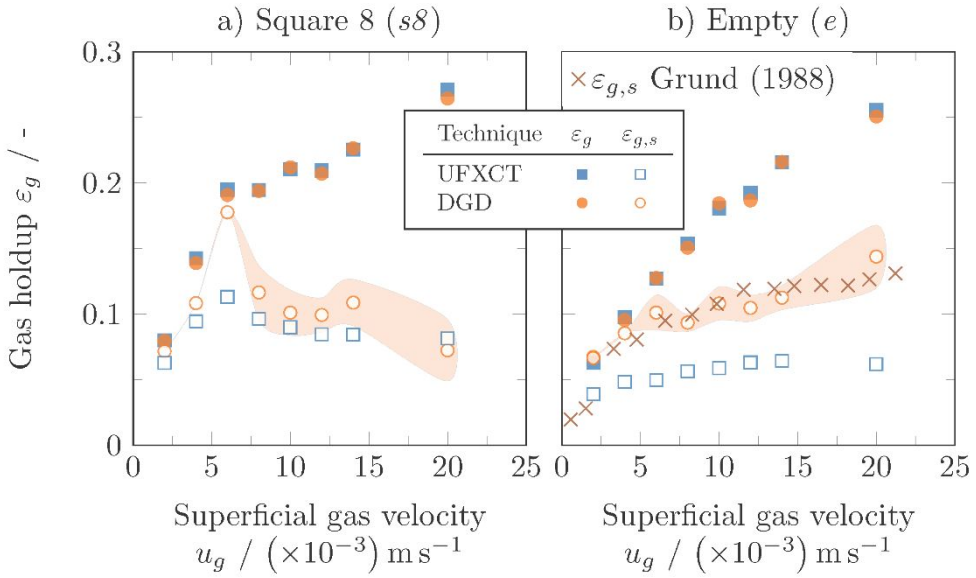

Figure 7: Comparison of total and small bubble class holdups obtained from UFXCT and DGD data as well as literature data (shaded area illustrates the DGD error range for the small bubble class holdup).

The shaded area illustrates the error range for the small bubble class holdup obtained via DGD caused by the different slopes (see Figure 4). The small bubble class data obtained via DGD (this work and from

Grund[30]) agree very well, however, deviate from the UFXCT results for the column with and without internals. Strongest deviations are observed for the transition between homogeneous and heterogeneous regime (0.03 m s^{-1} to 0.07 m s^{-1}). For the empty BCR, the DGD strongly overestimates the small bubble class holdup due to faster rising large bubbles. These large and fast-rising bubbles in the column center entrain a large portion of small bubbles within their wakes. For the internals, the formation of such large bubbles is suppressed, thus better agreement between the results of the two measurement techniques. Beyond the subjective slope determination, the following tasks limit the reliability of the DGD technique:

- accuracy of the disengagement profile, while large bubbles leave the column,
- no proper allocation of entrained small bubbles within the large bubbles' wakes,
- descending small bubbles, which follow the liquid circulation stream lines in the wall region after shut-off, and
- excess gas in the sparger chamber after shut off distort the DGD profile.

Thus, reliable classification based on UFXCT data is further utilized to analyze small and large bubble classes and their contribution in BCRs with and without internals. Accordingly, the threshold values in Table 2 are subsequently used to allocate the bubbles to small and large bubble classes and to further analysis their holdups and respective bubble rise velocities.

4.2 Large and small bubble holdups

Figure 8 summarizes small and large bubble class holdups for the experiments without and with internals (8 and 13 mm tubes). Furthermore, the correlations of Krishna and Ellenberger[29] and Wilkinson et al.[28] are applied (see Equations 9-17).

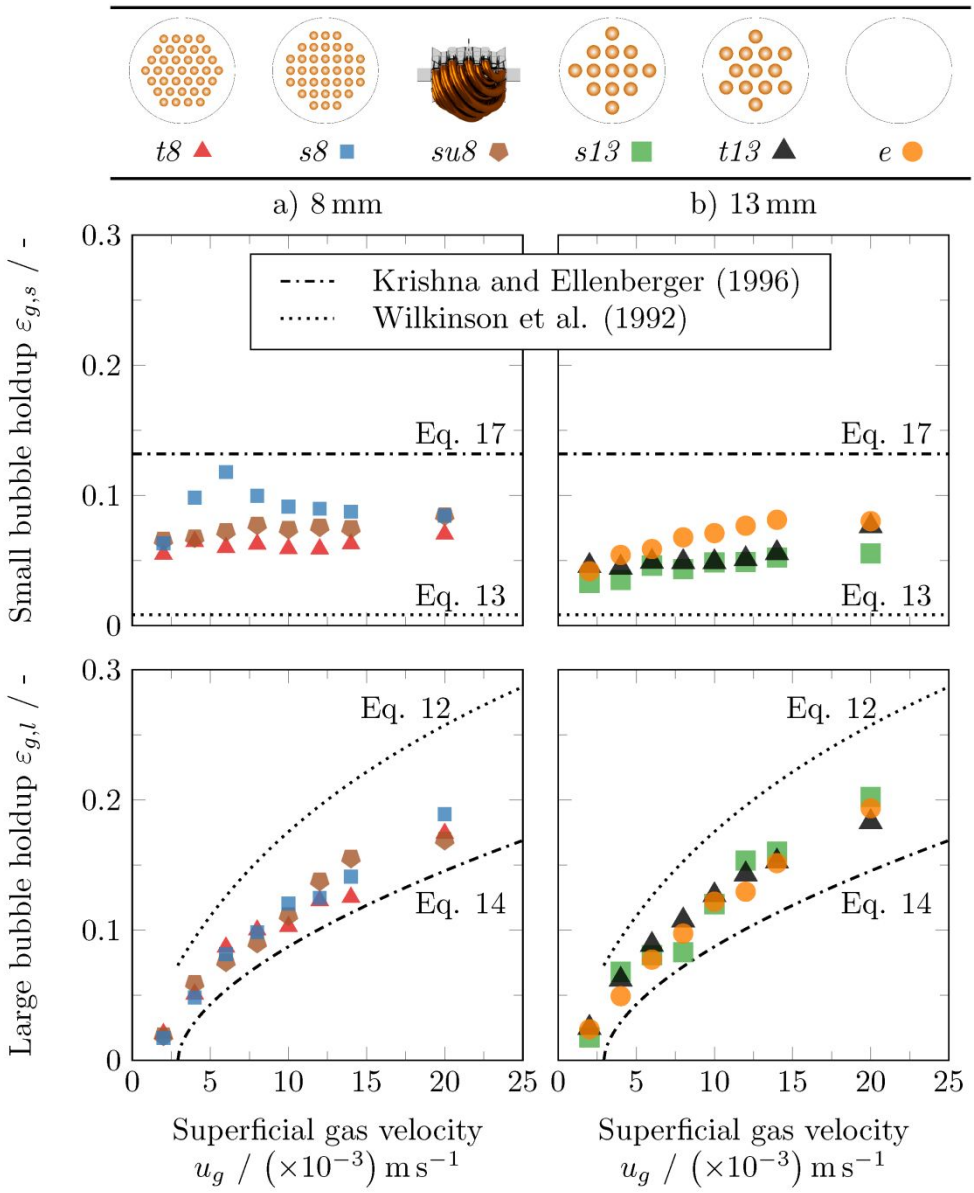

Figure 8: Small and large bubble class holdups internals with a) 8 mm tubes, b) 13 mm tubes and without internals as well as comparison with literature correlations.

Based on the model assumption of the TBCA, the small bubble class holdup contribution should be constant after the regime transition onset. This concept agrees fairly well with the measurements for all internals with 8 mm tubes. However, a distinctive peak is obtained for the Square 8 (*s8*) configuration, at regime transition, which is caused by higher breakup frequencies. For the internals with larger tubes (13 mm) and the empty column, the small bubble class holdups continuously increase with increasing superficial gas velocity, even though with small slope. It should be noted that the sub-channel area mainly controls the bubble size, which eventually determines the holdup slope[23,24]. For the empty bubble column, the holdup increases with the superficial gas velocity due to higher local turbulence[68]. Therefore, with

every formed large bubble, shearing effects play an important role, which increase the small bubble class holdup. Furthermore, the TBCA assumes that larges bubbles are not formed before the onset of the regime transition, which is evident from Figure 8. For 0.02 m s^{-1} the large bubble class holdup contribution is almost negligible. However, the large bubble class holdup increases sharply at 0.04 m s^{-1} and moderately thereafter for all investigated configurations.

The correlation developed by Wilkinson et al.[28] strongly underpredicts the small bubble class contribution, which was already discussed by Krishna and co-workers[29,37]. The correlation of Krishna and Ellenberger[29], however, overpredicts the small bubble holdup. The highest deviation is obtained for the configurations with the 13 mm tubes. Here, the larger sub-channels promote slightly larger bubbles, which leads to a lower small bubble class contribution. The deviations between experimental data and predictions from Krishna and Ellenberger[29] can be clearly attributed to the disadvantages associated with the DGD technique.

The large bubble class holdups fairly agree with the prediction by the correlation of Krishna and Ellenberger[29]. Logically, the over-prediction of the small bubble class results in under-predicted large bubble class holdups (and vice versa for the correlation of Wilkinson et al.[28]).

4.3 Bubble rise velocity

To evaluate the bubble rise velocity of small and large bubble classes, the respective distributions were determined based on the bubble pairing algorithm by Furuya et al.[64]. Descending bubbles were discarded from the data processing. It should be mentioned that the ratio of descending bubbles was always below 10 % and, thus, does not significantly bias the velocity distributions. The corresponding PDF of the large and small bubble velocity are shown in Figure 9 for Square 8 (*s8*) configuration and empty column at a superficial gas velocity of 0.20 m s^{-1}.

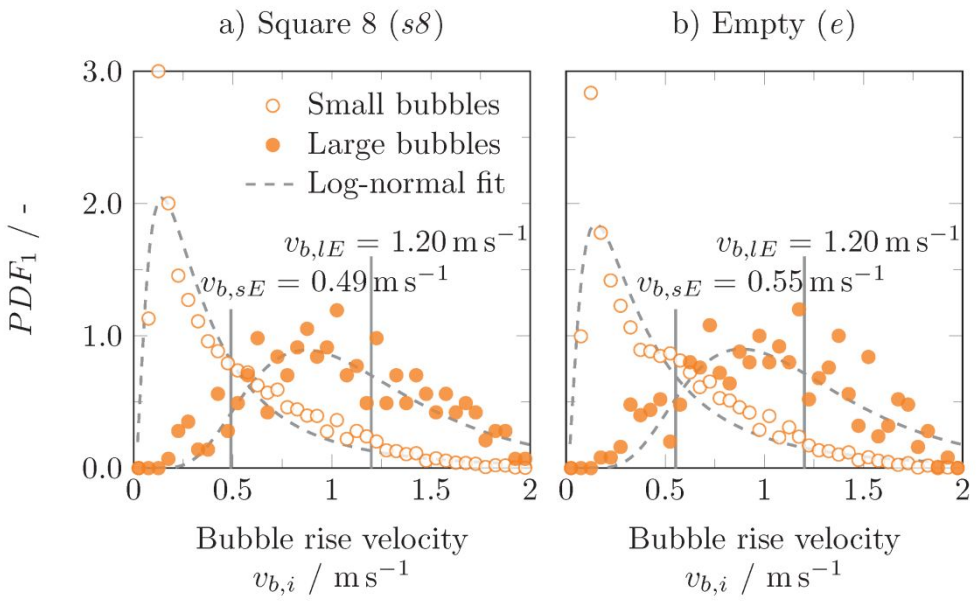

Figure 9: Class-specific bubble rise velocity based on the log-normal distribution at 0.20 m s^{-1} superficial gas velocity of for a) Square 8 (*s8*) configuration and b) empty column.

The expectation value for the bubble rise velocity, $v_{b,E}$, is obtained from the log-normal distribution (in analogy to Equations 22 and 23) of the small and large bubble velocity distributions. The bubble velocity distribution for the small bubble class is much narrower compared to the large bubble class with widely scattering size distribution (see Figure 5). The characteristic bubble rise velocities for small and large bubble classes are summarized in Figure 10.

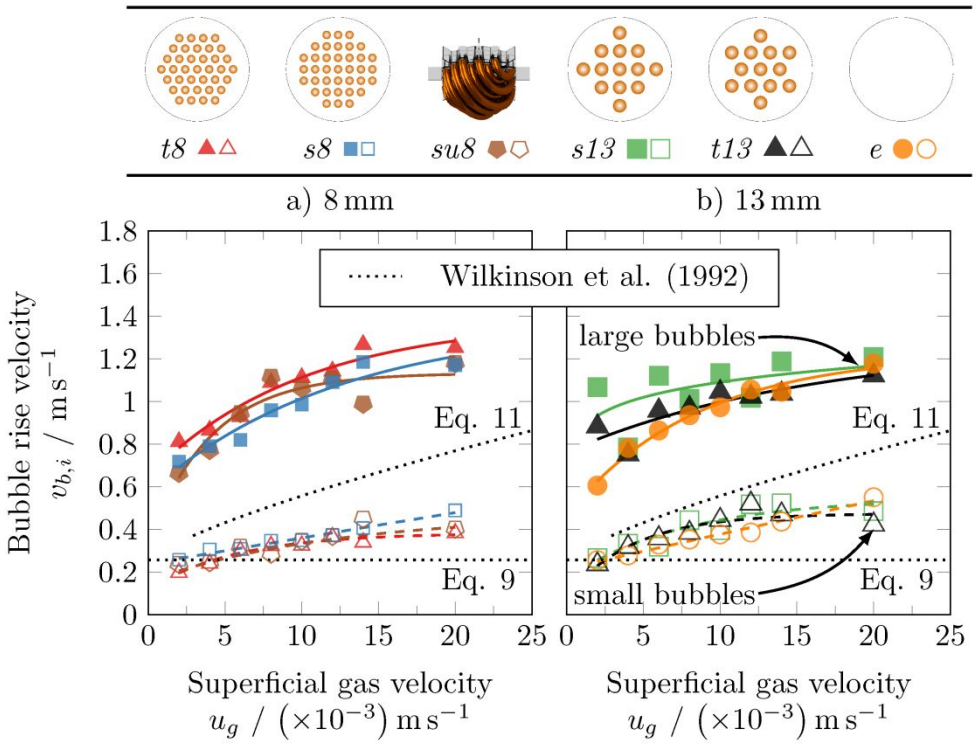

Figure 10: Characteristic bubble rise velocities of small and large bubble classes for internals with a) 8 mm tubes and b) 13 mm tubes as well as empty bubble column.

With increasing superficial gas velocity, both, small and large bubble class velocities increase regardless of the configurations. Furthermore, as the large bubble diameters are expanding with increasing gas velocity, higher rise velocities occur. Additionally, small bubbles are entrained within the large bubbles' wakes, which results in a faster small bubble class rise velocities, too. Therefore, contrary to the model assumptions by Wilkinson et al[28] and Krishna and Ellenberger[29], the small bubble rise velocity is increasing (as a result of the increasing average large bubble size).

The small bubbles' rise velocity again depends on the sub-channel area. Contrary to internals with larger sub-channels and empty column, small sub-channels limit the bubbles size and, thus, the rise velocity. On the other hand, the sub-channel size (flow friction) and the free wall region ratio determine the large bubble class rise velocity. The flow friction increases with decreasing sub-channel area (e.g. Triangular 8 (*t8*)), which leads to an increased bubble movement towards the column wall, where they form agglomerates (see Figure 6). This, in turn, accelerates the bubble coalescence near the wall, which results in fast-rising large bubbles. For large sub-channels, larger bubbles with a higher velocity are formed. For the empty column, the large bubble rise velocity is smaller compared to the configurations with internals as a result of the higher radial bubble exchanger, which is inhibited in BCRs with internals caused by the funneling or bubble caging effect.

Figure 10 also compares the determined velocities with the prediction of Wilkinson et al.[28]. Here, the large bubble class velocity determined experimentally wrongly falls together with the prediction of the small bubble class velocity

4.4 Determination of the regime transition onset

Typically, the onset of the regime transition is determined by means of Wallis plots[69], swarm velocity plots[70] or with stochastic methods[22]. Based on the TBCA, the average holdup can also be predicted using Equations 6 and 7. Here, the unknown regime transition velocity can be determined using the least square method based on available data for small and large bubble class rise velocity and the total gas holdup.

Table 3 summarizes the determined transition velocity for empty column and columns with internals. Nedeltchev et al.[22,65] used exact the same setup (empty BCR and Square 8 (*s8*) configuration) to determine the regime transitions via statistical methods and reported transition velocities of 0.04 m s^{-1} for the empty BCR and 0.06 m s^{-1} for the Square 8 (*s8*) configuration. The results obtained with the inverse calculation method agree perfectly well with the transitions proposed by Nedeltchev et al.[22,65]. Thus, the method can be considered reliable providing that data for total gas holdup and bubble rise velocities at heterogeneous flow conditions are available.

Table 3: Regime transition velocities determined for all configurations based on the TBCA model according to Equations 6 and 7.

Configuration	Transition velocity
Empty (*e*)	0.039 m s^{-1}
Square 8 (*s8*)	0.059 m s^{-1}
SquareU 8 (*su8*)	0.041 m s^{-1}
Triangular 8 (*t8*)	0.034 m s^{-1}
Square 13 (*s13*)	0.044 m s^{-1}
Triangular 13 (*t13*)	0.046 m s^{-1}

The results confirm that internals promote higher breakup frequencies and funneling effects that inhibit the large bubble formation, which, in turn, delays the regime transition. On the other hand, the Triangular 8 (*t8*) configuration promotes early onset of coalescence in the wall region due to an increased flow friction caused by small sub-channel areas.

4.5 New correlation for small and large bubble rise velocity and total gas holdup

The available correlations for small and large bubble rise velocity as well as for regime transition, large bubble class and total holdup do not properly account for the effects of the internals. In particular, the

distinct geometric parameters are not at all considered. The structure of new correlations follows the formulations used by Wilkinson et al.[28]. The area occupied by the internals, the sub-channel area as well as the hydraulic sub-channel diameter are the most significant parameters for the hydrodynamics of BCRs with internals[23–25] and considered in terms of free area ratio and 'sub-channel area'-to-'sub-channel hydraulic diameter'-ratio in a dimensionless manner. Since gas and liquid properties were not varied in this study, same exponents as proposed by Wilkinson et al.[28] were kept for the terms referring to fluid properties.

The new correlation for the small bubble class rise velocity is

$$v_{b,s} = 52.25\frac{\sigma_l}{\eta_l}\left(\frac{{\sigma_l}^3\rho_l}{g\eta_l}\right)^{-0.273}\left(\frac{\rho_l}{\rho_g}\right)^{0.03}\left(\frac{u_g^2}{gD}\right)^{0.16}(1-A_c)^{7.8}\left(\frac{A_s}{d_h^2}\right)^{0.5}. \quad (25)$$

The large bubble class rise velocity is described as

$$v_{b,l} = \frac{\sigma_l}{\eta_l}\left[\frac{\eta_l v_{b,s}}{\sigma_l} + 0.02\left(\frac{\eta_l(u_g-u_{trans})}{\sigma_l}\right)^{0.032}\left(\frac{{\sigma_l}^3\rho_l}{g\eta_l}\right)^{-0.077}\left(\frac{\rho_l}{\rho_g}\right)^{0.077}(1-A_c)^{-2.3}\left(\frac{A_s}{d_h^2}\right)^{-0.16}\right], \quad (26)$$

where the transition velocity is correlated as

$$u_{trans} = 25.01\bar{v}_{b,s}\exp\left(-198.33\rho_g^{-0.61}\eta_l^{0.5}{\sigma_l}^{0.11}\right)(1-A_c)^{4.63}\left(\frac{A_s}{d_h^2}\right)^{-0.23}. \quad (27)$$

The large bubble class holdup is expressed as

$$\varepsilon_{g,l} = 1.95D^{-0.18}u_g^{0.87}(1-A_c)^{4.85}\left(\frac{A_s}{d_h^2}\right)^{-0.16}. \quad (28)$$

The predictions of the new correlations are compared with the experimental data in Figure 11 by means of parity plots.

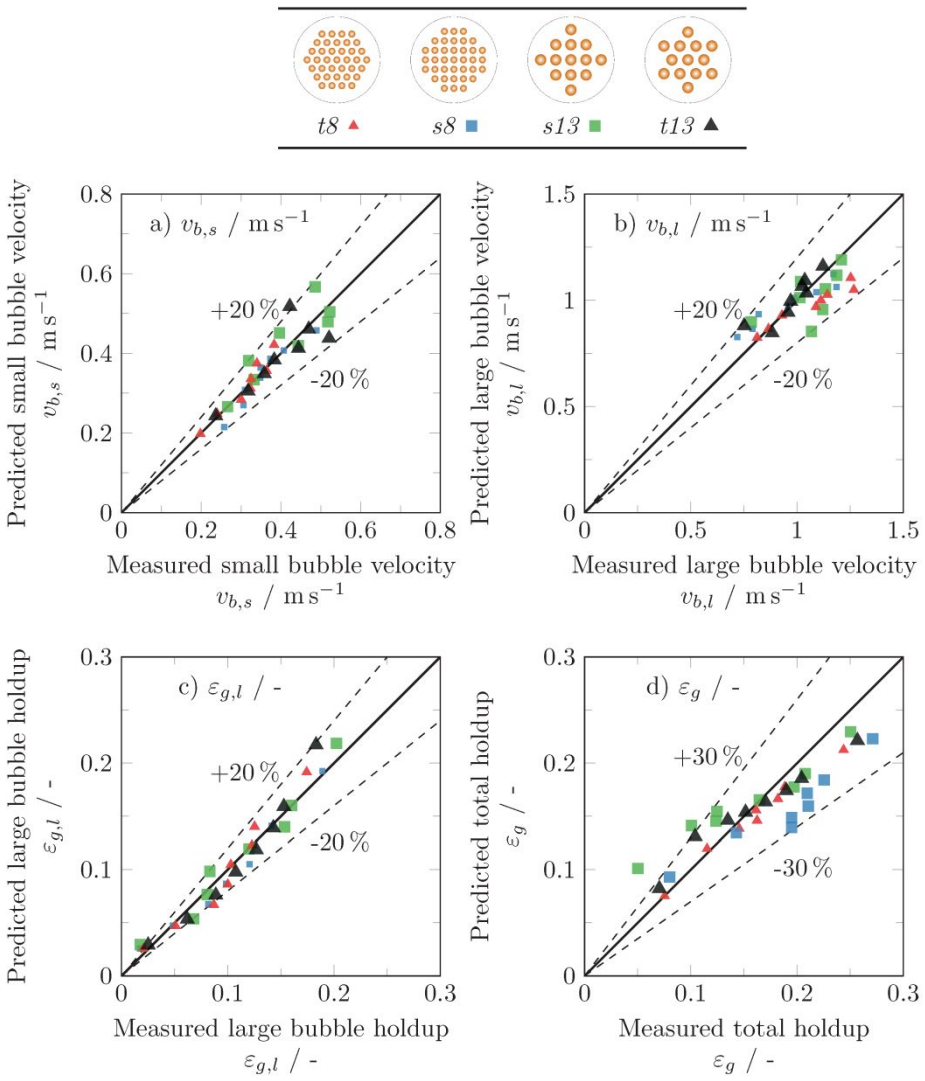

Figure 11: Comparison of experimental data with predictions of the new correlations (Equations 25 to28) for a) small and b) large bubble class rise velocities and c) large bubble class holdup as well as d) total gas holdup (Equations 6 and 7).

Predicted and measured data for bubble velocities and large bubble class holdup agree well with an average error range of ±20 %. By the established equations, the total gas holdup can be calculated using the TBCA formulations described in Equations 6 and 7. The total gas holdup prediction agrees fairly well with an accuracy of ±30 %.

5 Conclusions

The two-bubble class approach (TBCA) was applied to hydrodynamic data of BCRs with dense internals. Furthermore, the small and large bubble class correlations proposed by Wilkinson et al.[28], Krishna and Ellenberger[29] as well as the experimental data of Grund[30] have been tested against the measurement data

of this work. As an alternative approach to the widely applied but rather inaccurate dynamic gas disengagement technique (DGD), ultrafast X-ray tomography (UFXCT) was used to divide bubble classes based on characteristic data of the determined bubble size and bubble velocity distributions. These characteristic data were further utilized to predict the regime transition velocity based on the TBCA.

Eventually, new correlations for small and large bubble rise velocity, large bubble holdup as well as the regime transition considering the most crucial tube bundle design parameters for BCRs with internals (sub-channel area, hydraulic diameter and occlusion area) have been developed and successfully tested for the prediction of the total gas holdup.

Acknowledgement

The authors gratefully acknowledge the European Research Council (ERC StG, No. 307360) for financial support.

Nomenclature

Abbreviations

BCR	bubble column reactor
BSD	bubble size distribution
DGD	dynamic gas disengagement
PDF	probability density function
TBCA	two-bubble class approach
UFXCT	Ultrafast X-ray computed tomography

Symbols

A_c	covered fraction of the cross-sectional area, %
A_s	sub-channel area, m^2
D	column diameter, m
d_e	equivalent bubble diameter, m
$d_{e,E}$	expectation value for the equivalent bubble diameter of the log-normal distribution, m
d_h	hydraulic sub-channel diameter, m
d_o	tube outer diameter, m
g	earth acceleration, m s^{-2}
l_V	voxel edge length, m
N	number of tubes, -
N_f	number of measurement frames, -

N_{pi}	number of pixels within the circular cross-section in x and y direction, -
n_b	number of bubbles, -
P	pitch, m
R	column radius, m
r	radial coordinate, m
r_v	bubble volume change from first to second plane, -
$u_{b,l}$	superficial large bubble class velocity, m s^{-1}
$u_{b,s}$	superficial small bubble class velocity, m s^{-1}
u_g	superficial gas velocity, m s^{-1}
$u_{g,l}$	large bubble class superficial velocity, m s^{-1}
$u_{g,s}$	small bubble class superficial velocity, m s^{-1}
V_b	bubble volume, m^3
v_b	bubble rise velocity, m s^{-1}
$v_{b,l}$	large bubble class rise velocity, m s^{-1}
$v_{b,lE}$	expectation value for the large bubble rise velocity of the log-normal distribution, m s^{-1}
$v_{b,s}$	small bubble class rise velocity, m s^{-1}
$\overline{v}_{b,s}$	average small bubble class rise velocity, m s^{-1}
$v_{b,sE}$	expectation value for the small bubble rise velocity of the log-normal distribution, m s^{-1}

Greek symbols

$\alpha_{i,j,k}$	phase fraction, -
$\Delta P/\Delta H$	specific pressure difference, N m^{-3}
Δt	time difference, s
ε_g	total gas holdup, -
$\varepsilon_{g,l}$	large bubble class holdup, -
$\varepsilon_{g,s}$	small bubble class holdup, -
ε_{trans}	gas holdup at regime transition onset, -
η_l	liquid viscosity, pas
μ	coefficient of the log-normal distribution, -
$\boldsymbol{\mu_e}$	empty bubble column reference, -
$\boldsymbol{\mu_f}$	full bubble column reference, -
$\boldsymbol{\mu_n}$	normalized data, -
$\boldsymbol{\mu_r}$	reference data, -
ρ_g	gas phase density, kg m^{-3}
ρ_l	liquid phase density, kg m^{-3}
σ	coefficient of the log-normal distribution, -

σ_l liquid surface tension, N m^{-1}

Bibliography

1. Deckwer W-D, Schumpe A. Improved tools for bubble column reactor design and scale-up. *Chemical Engineering Science*. 1993;48(5):889-911. doi:http://dx.doi.org/10.1016/0009-2509(93)80328-N

2. Schlüter S, Steiff A, Weinspach P-M. Heat transfer in two- and three-phase bubble column reactors with internals. *Chemical Engineering and Processing: Process Intensification*. 1995;34(3):157-172. doi:http://dx.doi.org/10.1016/0255-2701(94)04002-8

3. Rollbusch P, Bothe M, Becker M, et al. Bubble columns operated under industrially relevant conditions – Current understanding of design parameters. *Chemical Engineering Science*. 2015;126:660-678. doi:http://dx.doi.org/10.1016/j.ces.2014.11.061

4. Berg S. Zur Gasgehaltsverteilung und zum Verweilzeitverhalten der Gasphase in Blasensäulen mit längsangeströmten Rohrbündeleinbauten. 1993.

5. Berg S, Steiff A, Weinspach P-M. Gasgehaltsverteilung und Verweilzeitverhalten der Gasphase in Blasensäulen mit längsangeströmten Rohrbündeleinbauten. *Chemie Ingenieur Technik*. 1994;66(5):724-727. doi:10.1002/cite.330660522

6. Youssef AA, Al-Dahhan MH, Duduković MP. Bubble Columns with Internals: A Review. *International Journal of Chemical Reactor Engineering*. 2013;11(1):169-223. //www.degruyter.com/view/j/ijcre.2013.11.issue-1/ijcre-2012-0023/ijcre-2012-0023.xml.

7. Jasim A. The impact of heat exchanging internals on hydrodynamics of bubble column reactor. 2016. http://scholarsmine.mst.edu/cgi/viewcontent.cgi?article=8506&context=masters_theses.

8. Bernemann K. Zur Fluiddynamik und zum Vermischungsverhalten der flüssigen Phasen in Blasensäulen mit längsangeströmten Rohrbündeln. 1989.

9. Hamed M. Hydrodynamics Mixing and Mass Transfer in Bubble Columns with Internals. 2012.

10. Youssef AA. Fluid Dynamics and Scalue-Up of Bubble Columns with Internals. 2010.

11. Mesfer MKA, Sultan AJ, Al-Dahhan MH. Impacts of dense heat exchanging internals on gas holdup cross-sectional distributions and profiles of bubble column using gamma ray Computed Tomography (CT) for FT synthesis. *Chemical Engineering Journal*. 2016;300:317-333. doi:http://dx.doi.org/10.1016/j.cej.2016.04.075

12. Guan X, Gao Y, Tian Z, Wang L, Cheng Y, Li X. Hydrodynamics in bubble columns with pin-fin tube internals. *Chemical Engineering Research and Design*. 2015;102:196-206. doi:10.1016/j.cherd.2015.06.028

13. Larachi F, Desvigne D, Donnat L, Schweich D. Simulating the effects of liquid circulation in bubble columns with internals. *Chemical Engineering Science*. 2006;61(13):4195-4206. doi:http://dx.doi.org/10.1016/j.ces.2006.01.053

14. Kalaga DV, Y. A, Goswami S, et al. Comparative analysis of liquid hydrodynamics in a co-current flow-through bubble column with densely packed internals via radiotracing and Radioactive Particle Tracking (RPT). *Chemical Engineering Science*. 2017;170:332-346. doi:https://doi.org/10.1016/j.ces.2017.02.022

15. Chen J, Li F, Degaleesan S, et al. Fluid dynamic parameters in bubble columns with internals. *Chemical Engineering Science*. 1999;54(13):2187-2197. doi:http://dx.doi.org/10.1016/S0009-2509(99)00003-2

16. Westermeyer-Benz H. Wärmeübergang und Gasgehalt in zwei-und dreiphasig betriebenen Blasensäulenreaktoren mit längseingebauten Rohren. 1992.

17. Korte H-J. Wärmeübergang in Blasensäulen mit und ohne Einbauten. 1987.

18. Berg S, Schlüter S. Rückvermischung in Blasensäulen mit Einbauten. *Chemie Ingenieur Technik*. 1995;67(3):289-299. doi:10.1002/cite.330670305

19. Bernemann K, Steiff A, Weinspach P-M. Zum Einfluß von längsangeströmten Rohrbündeln auf die großräumige Flüssigkeitsströmung in Blasensäulen. *Chemie Ingenieur Technik*. 1991;63(1):76-77. doi:10.1002/cite.330630120

20. Youssef AA, Al-Dahhan MH. Impact of Internals on the Gas Holdup and Bubble Properties of a Bubble Column. *Industrial and Engineering Chemistry Research*. 2009;48(17):8007-8013. doi:10.1021/ie900266q

21. Youssef AA, Hamed ME, Al-Dahhan MH, Duduković MP. A new approach for scale-up of bubble column reactors. *Chemical Engineering Research and Design*. 2014;92(9):1637-1646. doi:10.1016/j.cherd.2013.12.011

22. Nedeltchev S, Möller F, Schubert M. Effect of Heat Exchanger Internals on the Main Transition Velocities in a Bubble Column. In: *Proceeding Third International SymposiumMultiscaleMultiphaseProcessEngineering(MMPE)*. ; 2017.

23. Möller F, Lau YM, Seiler T, Hampel U, Schubert M. A study on the influence of the tube layout on sub-channel hydrodynamics in a bubble column with internals. *Chemical Engineering Science*. 2018;179:265-283. doi:https://doi.org/10.1016/j.ces.2018.01.008

24. Lau YM, Möller F, Hampel U, Schubert M. Ultrafast X-ray tomographic imaging of multiphase flow in bubble columns – Part 2: Characterisation of bubbles in the dense regime. *International Journal of Multiphase Flow*. 2018. doi:https://doi.org/10.1016/j.ijmultiphaseflow.2018.02.009

25. Möller F, MacIsaac A, Lau YM, Schleicher E, Hampel U, Schubert M. Advanced Analysis of Liquid Dispersion and Gas-Liquid Mass Transfer in a Bubble Column with Dense Vertical Internals. *Chemical Engineering Research and Design*. 2018.

26. Kagumba MOO, Al-Dahhan MH. Impact of Internals Size and Configuration on Bubble Dynamics in Bubble Columns for Alternative Clean Fuels Production. *Industrial & Engineering Chemistry Research*. 2015;54(4):1359-1372. doi:10.1021/ie503490h

27. Kagumba MOO. Heat transfer and Bubble Dynamics in Bubble and slurry Bubble column with internals for Fischer-Tropsch synthesis of clean alternative fuels and chemicals. 2013.

28. Wilkinson PM, Spek AP, Dierendonck LL van. Design parameters estimation for scale-up of high-pressure bubble columns. *AIChE Journal*. 1992;38(4):544-554. doi:10.1002/aic.690380408

29. Krishna R, Ellenberger J. Gas holdup in bubble column reactors operating in the churn-turbulent flow regime. *AIChE Journal*. 1996;42(9):2627-2634. doi:10.1002/aic.690420923

30. Grund G. Hydrodynamische Parameter und Stoffaustauscheigenschaften in Blasensäulen mit organischen Medien. 1988.

31. Deckwer WD. *BubbleColumnReactors*. John Wiley & Sons Inc; 1992.

32. Nedeltchev S, Shaikh A. A new method for identification of the main transition velocities in multiphase reactors based on information entropy theory. *Chemical Engineering Science*. 2013;100:2-14. doi:http://dx.doi.org/10.1016/j.ces.2013.03.039

33. Shaikh A, Al-Dahhan MH. A Review on Flow Regime Transition in Bubble Columns. *International Journal of Chemical Reactor Engineering*. 2007;5. https://www.degruyter.com/view/j/ijcre.2007.5.1/ijcre.2007.5.1.1368/ijcre.2007.5.1.1368.xml.

34. Guan X, Yang N. CFD simulation of pilot-scale bubble columns with internals: Influence of interfacial forces. *Chemical Engineering Research and Design*. 2017;126:109-122. doi:https://doi.org/10.1016/j.cherd.2017.08.019

35. Shah YT, Kelkar BG, Godbole SP, Deckwer W-D. Design parameters estimations for bubble column reactors. *AIChE Journal*. 1982;28(3):353-379. doi:10.1002/aic.690280302

36. Swart JWAD, Vliet RE van, Krishna R. Size, structure and dynamics of "large" bubbles in a two-dimensional slurry bubble column. *Chemical Engineering Science*. 1996;51(20):4619-4629. doi:https://doi.org/10.1016/0009-2509(96)00265-5

37. Krishna R, Urseanu MI, Baten JM van, Ellenberger J. Rise velocity of a swarm of large gas bubbles in liquids. *Chemical Engineering Science*. 1999;54(2):171-183. doi:http://dx.doi.org/10.1016/S0009-2509(98)00245-0

38. Shah YT, Joseph S, Smith DN, Ruether JA. Two-bubble class model for churn turbulent bubble-column reactor. *Industrial & Engineering Chemistry Process Design and Development*. 1985;24(4):1096-1104. doi:10.1021/i200031a034

39. Degaleesan S, Roy S, Kumar SB, Duduković MP. Liquid mixing based on convection and turbulent dispersion in bubble columns. *Chemical Engineering Science*. 1996;51(10):1967-1976. doi:http://dx.doi.org/10.1016/0009-2509(96)00054-1

40. Degaleesan MP S.and Duduković. Liquid backmixing in bubble columns and the axial dispersion coefficient. *AIChE Journal*. 1998;44(11):2369-2378. doi:10.1002/aic.690441105

41. Degaleesan S, Dudukovic MP, Toseland BA, Bhatt BL. A Two-Compartment Convective-Diffusion Model for Slurry Bubble Column Reactors. *Industrial & Engineering Chemistry Research*. 1997;36(11):4670-4680. doi:10.1021/ie970200s

42. Jiang X, Yang N, Zhu J, Yang B. On the single and two-bubble class models for bubble column reactors. *Chemical Engineering Science*. 2015;123:514-526.

43. Gupta P, Al-Dahhan MH, Dudukovic MP, Toseland BA. Comparison of single- and two-bubble class gas–liquid recirculation models — application to pilot-plant radioactive tracer studies during methanol synthesis. *Chemical Engineering Science*. 2001;56(3):1117-1125. doi:https://doi.org/10.1016/S0009-2509(00)00329-8

44. Maretto C, Krishna R. Design and optimisation of a multi-stage bubble column slurry reactor for Fischer–Tropsch synthesis. *Catalysis Today*. 2001;66(2):241-248. doi:https://doi.org/10.1016/S0920-5861(00)00626-X

45. Grund G, Schumpe A, Deckwer W-D. Gas-Liquid mass transfer in a bubble column with organic liquids. *Chemical Engineering Science*. 1992;47(13):3509-3516. doi:https://doi.org/10.1016/0009-2509(92)85064-I

46. Basha OM, Morsi BI. Novel Approach and Correlation for Bubble Size Distribution in a Slurry Bubble Column Reactor Operating in the Churn–Turbulent Flow Regime. *Industrial & Engineering Chemistry Research*. 2018;57(16):5705-5716. doi:10.1021/acs.iecr.8b00543

47. Li H, Prakash A. Influence of slurry concentrations on bubble population and their rise velocities in a three-phase slurry bubble column. *Powder Technology*. 2000;113(1):158-167. doi:https://doi.org/10.1016/S0032-5910(00)00228-X

48. Han C, Guan X, Yang N. Structure Evolution and Demarcation of Small and Large Bubbles in Bubble Columns. *Industrial & Engineering Chemistry Research*. 2018;57(25):8529-8540. doi:10.1021/acs.iecr.8b00703

49. Reilly IG, Scott DS, Debruijn TJW, Macintyre D. The role of gas phase momentum in determining gas holdup and hydrodynamic flow regimes in bubble column operations. *The Canadian Journal of Chemical Engineering*. 1994;72(1):3-12. doi:10.1002/cjce.5450720102

50. Thulukkanam K. *HeatExchangerDesignHandbook*. 2nd Edition. CRC Press; 2013.

51. Li H, Prakash A. Survey of heat transfer mechanisms in a slurry bubble column. *The Canadian Journal of Chemical Engineering*. 2001;79(5):717-725. doi:10.1002/cjce.5450790503

52. Bieberle M, Barthel F, Hoppe D, et al. Ultrafast electron beam X-ray computed tomography for 2D and 3D two-phase flow imaging. In: *2012IEEEInternationalConference Imaging SystemsTechniquesProceedings*. ; 2012:605-610. doi:10.1109/IST.2012.6295548

53. Bieberle M, Barthel F, Menz H-J, Mayer H-G, Hampel U. Ultrafast three-dimensional x-ray computed tomography. *Applied Physics Letters*. 2011;98(3):034101. doi:10.1063/1.3534806

54. Bieberle M, Fischer F, Schleicher E, et al. Ultrafast limited-angle-type x-ray tomography. *Applied Physics Letters*. 2007;91(12):123516. doi:10.1063/1.2787879

55. Möller F, Seiler T, Lau YM, et al. Performance comparison between different sparger plate orifice patterns: Hydrodynamic investigation using ultrafast X-ray tomography. *Chemical Engineering Journal*. 2017;316:857-871. doi:http://dx.doi.org/10.1016/j.cej.2017.01.114

56. Wagner M, Barthel F, Zalucky J, Bieberle M, Hampel U. Scatter analysis and correction for ultrafast X-ray tomography. *Philosophical Transactions of the Royal Society of London A: Mathematical, Physical and Engineering Sciences*. 2015;373(2043). doi:10.1098/rsta.2014.0396

57. Bieberle M, Barthel F. Combined phase distribution and particle velocity measurement in spout fluidized beds by ultrafast X-ray computed tomography. *Chemical Engineering Journal*. 2016;285:218-227. doi:https://doi.org/10.1016/j.cej.2015.10.003

58. Banowski M, Beyer M, Szalinski L, Lucas D, Hampel U. Comparative study of ultrafast X-ray tomography and wire-mesh sensors for vertical gas–liquid pipe flows. *Flow Measurement and Instrumentation*. 2017;53, Part A:95-106. doi:https://doi.org/10.1016/j.flowmeasinst.2016.02.001

59. Lau YM, Müller K, Azizi S, Schubert M. Voronoï analysis of bubbly flows via ultrafast X-ray tomographic imaging. *Experiments in Fluids*. 2016;57(35):(57:35) 1-12. doi:10.1007/s00348-016-2118-8

60. Azizi S, Yadav A, Lau YM, Hampel U, Roy S, Schubert M. On the experimental investigation of gas-liquid flow in bubble columns using ultrafast X-ray tomography and radioactive particle tracking. *Chemical Engineering Science*. 2017;170(Supplement C):320-331. doi:https://doi.org/10.1016/j.ces.2017.02.015

61. Banowski M, Lucas D, Szalinski L. A new algorithm for segmentation of ultrafast X-ray tomographed gas-liquid flows. *International Journal of Thermal Sciences*. 2015;90(Complete):311-322. doi:10.1016/j.ijthermalsci.2014.12.015

62. Lau YM, Hampel U, Schubert M. Ultrafast X-ray tomographic imaging of multiphase flow in bubble columns - Part 1: Image processing and reconstruction comparison. *International Journal of Multiphase Flow*. 2018;104:258-271. doi:https://doi.org/10.1016/j.ijmultiphaseflow.2018.02.010

63. Banowski M, Patmonoaji A, Lucas D, Hampel U. A novel fuzzy-logic based method for determination of individual bubble velocity and size from dual-plane ultrafast X-ray tomography data of two-phase flow. *International Journal of Multiphase Flow*. 2017;96:144-160. doi:http://dx.doi.org/10.1016/j.ijmultiphaseflow.2017.07.012

64. Furuya M, Kanai T, Arai T, et al. Three-dimensional velocity vector determination algorithm for individual bubble identified with Wire-Mesh Sensors. *Nuclear Engineering and Design*. 2017. doi:https://doi.org/10.1016/j.nucengdes.2017.06.022

65. Nedeltchev S, Möller F, Hampel U, Schubert M. Flow Regime Transitions in a Bubble Column with Internals Based On a Novel Approach. *Chemical Engineering Journal Japan*. 2018. doi:10.1252/jcej.17we292

66. Maretto C, Piccolo V. Fischer-Tropsch process with a multistage bubble column reactor. October 1998. https://www.google.com/patents/US5827902.

67. Chen RC, Reese J, Fan LS. Flow structure in a three-dimensional bubble column and three-phase fluidized bed. *AIChE Journal*. 1994;40(7):1093-1104. doi:10.1002/aic.690400702

68. Joshi JB, Vitankar VS, Kulkarni AA, Dhotre MT, Ekambara K. Coherent flow structures in bubble column reactors. *Chemical Engineering Science*. 2002;57(16):3157-3183. doi:https://doi.org/10.1016/S0009-2509(02)00192-6

69. Wallis GB. *OnedimensionalTwophaseFlow*. New York: McGraw-Hill; 1969.

70. Besagni G, Inzoli F. Bubble size distributions and shapes in annular gap bubble column. *Experimental Thermal and Fluid Science*. 2016;74:27-48. doi:https://doi.org/10.1016/j.expthermflusci.2015.11.020

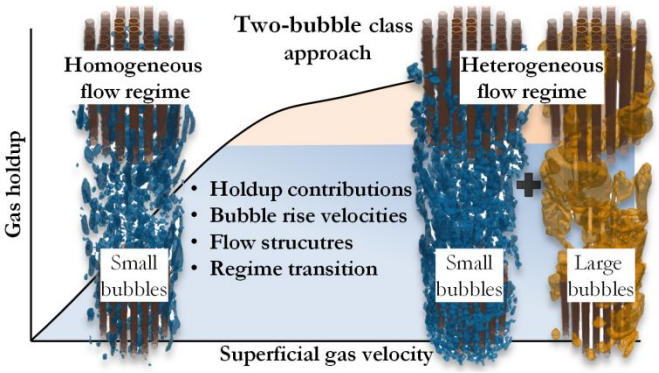

Figure 12: Graphical abstract

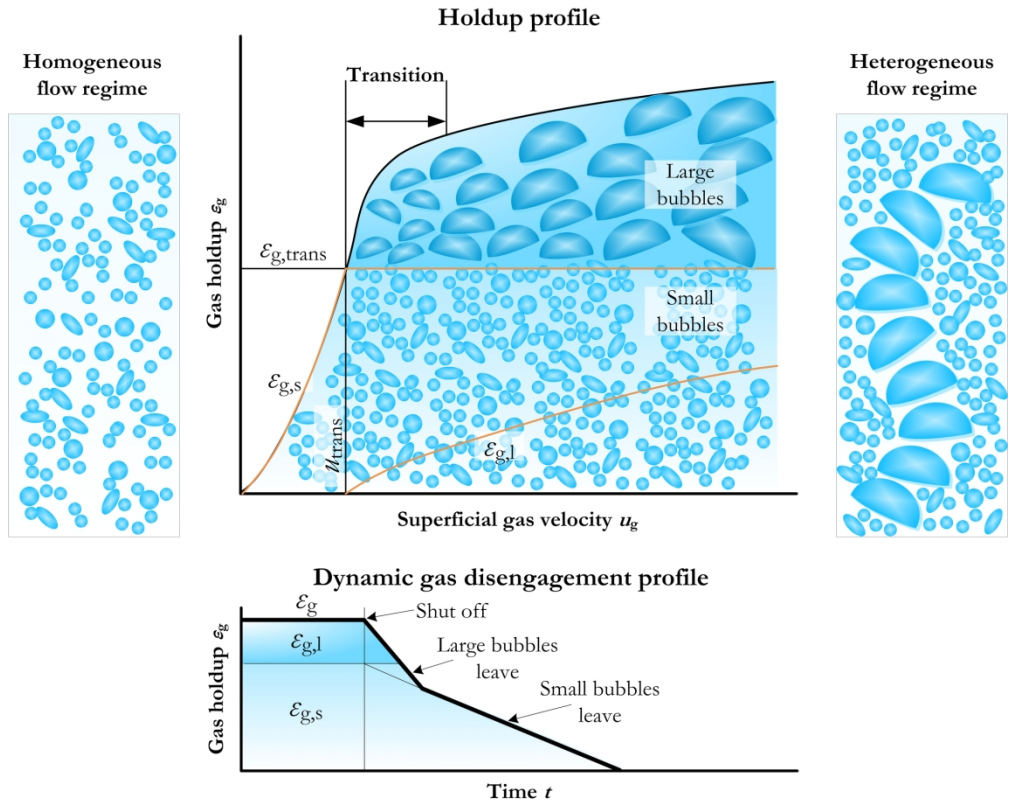

Figure 1: Illustration of TBCA with characteristic flow regimes and gas holdup profile in the upper row and DGD profile below for the determination of regime transition and bubble class holdups according to Grund30.

190x153mm (300 x 300 DPI)

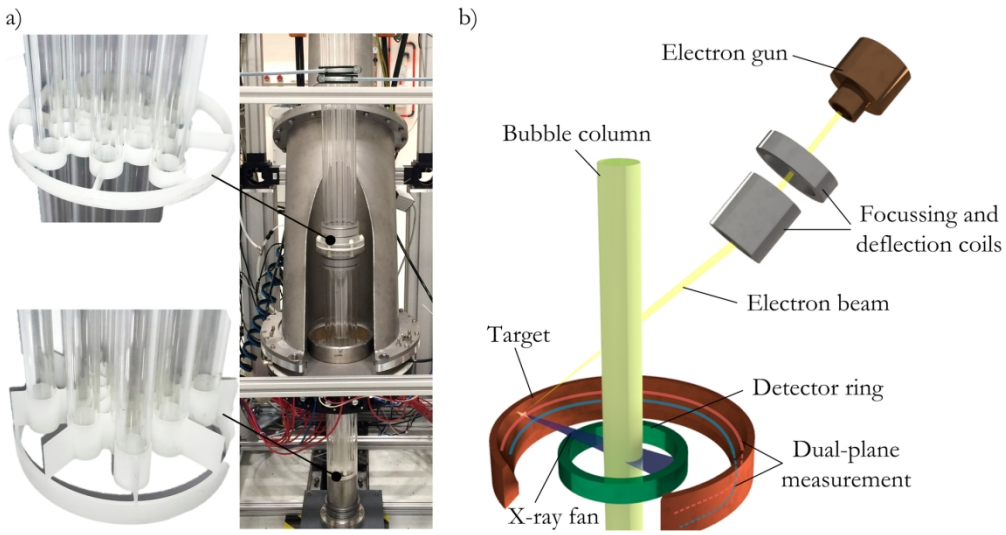

Figure 2: a) Photograph of the setup with images of the 3D-printed spacers and bottom parts as well as b) a schematic and rendered view of the UFXCT facility.

168x90mm (300 x 300 DPI)

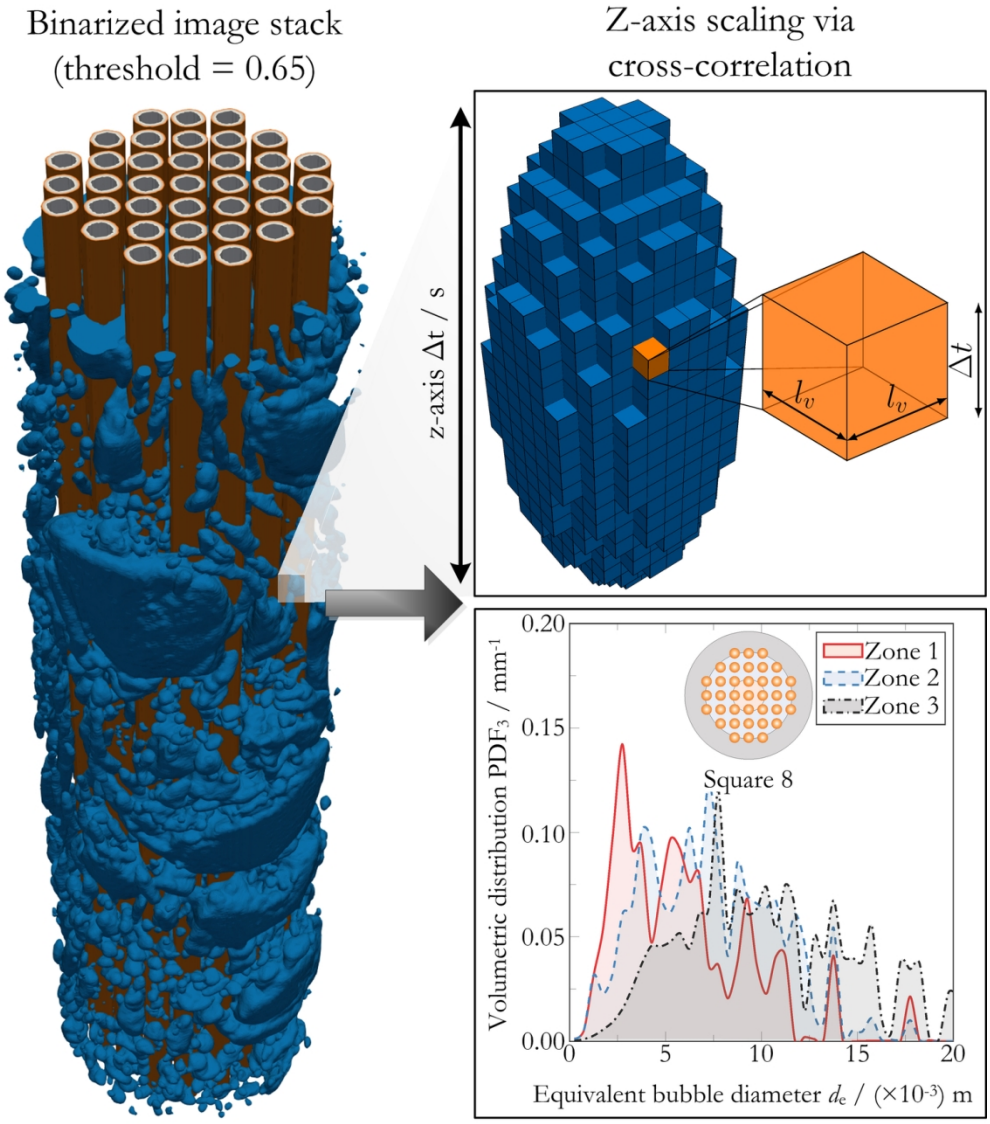

Figure 3: Schematic flow chart for the determination of bubble characteristics from binarized image stacks.

130x149mm (300 x 300 DPI)

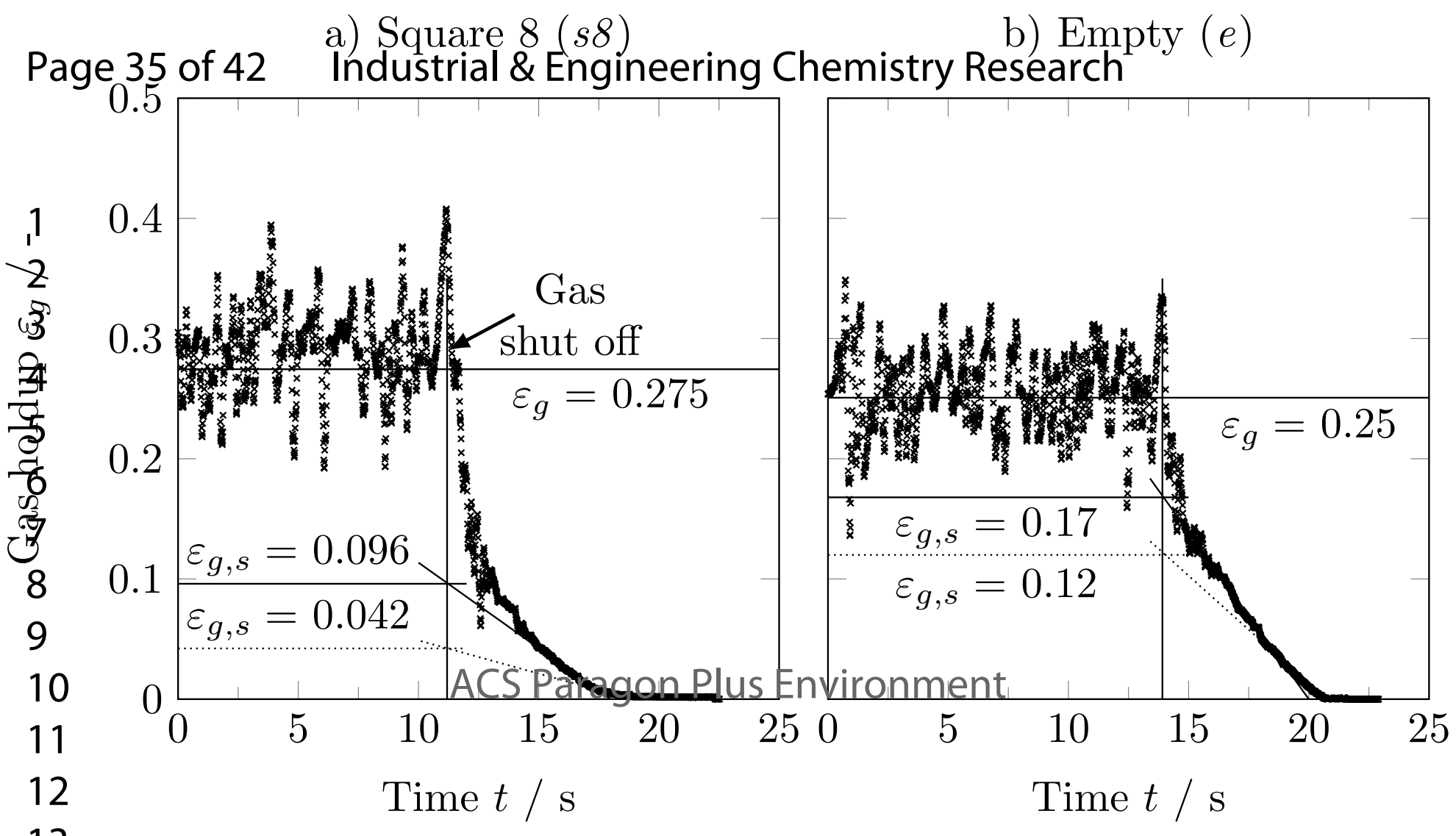

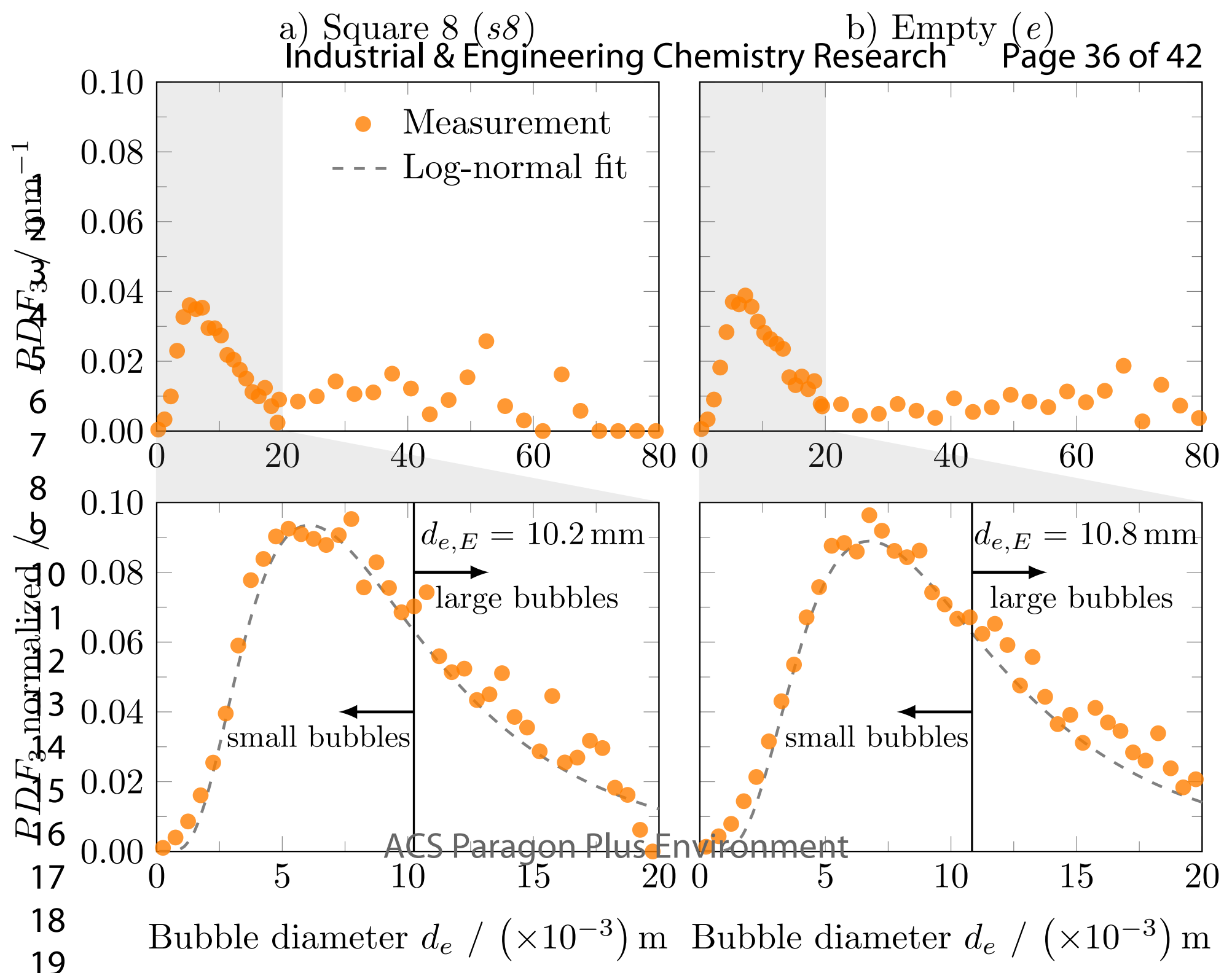

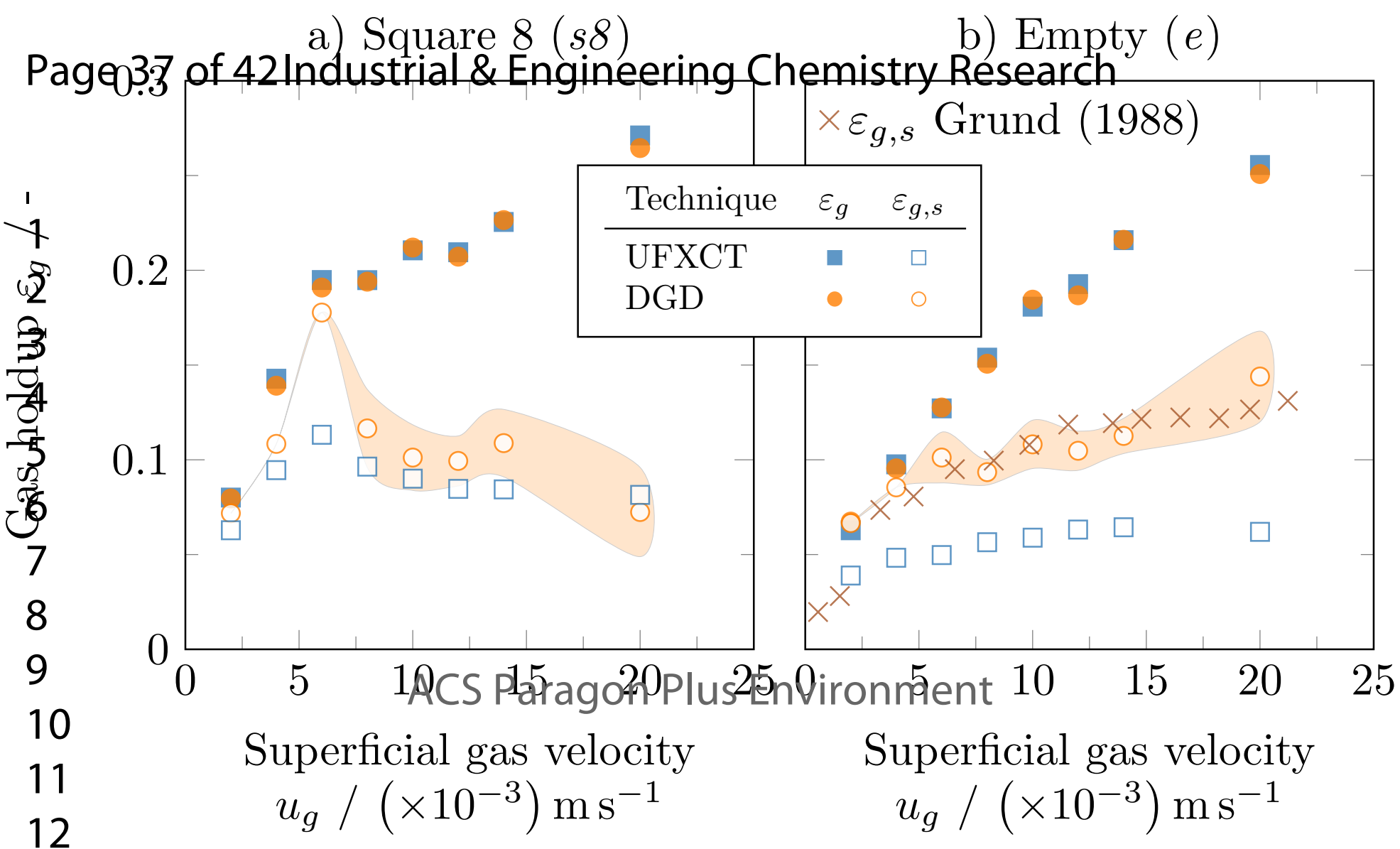

a) 8 mm

b) 13 mm

Small bubble holdup $\varepsilon_{g,1}$ / -

Large bubble holdup $\varepsilon_{g,2}$ / -

Krishna and Ellenberger (1996)

Wilkinson et al. (1992)

Eq. 17

Eq. 13

Eq. 12

Eq. 14

0.3

0.2

0.1

0

0

5

10

15

20

25

Superficial gas velocity
u_g / $(\times 10^{-3})$ m s^{-1}

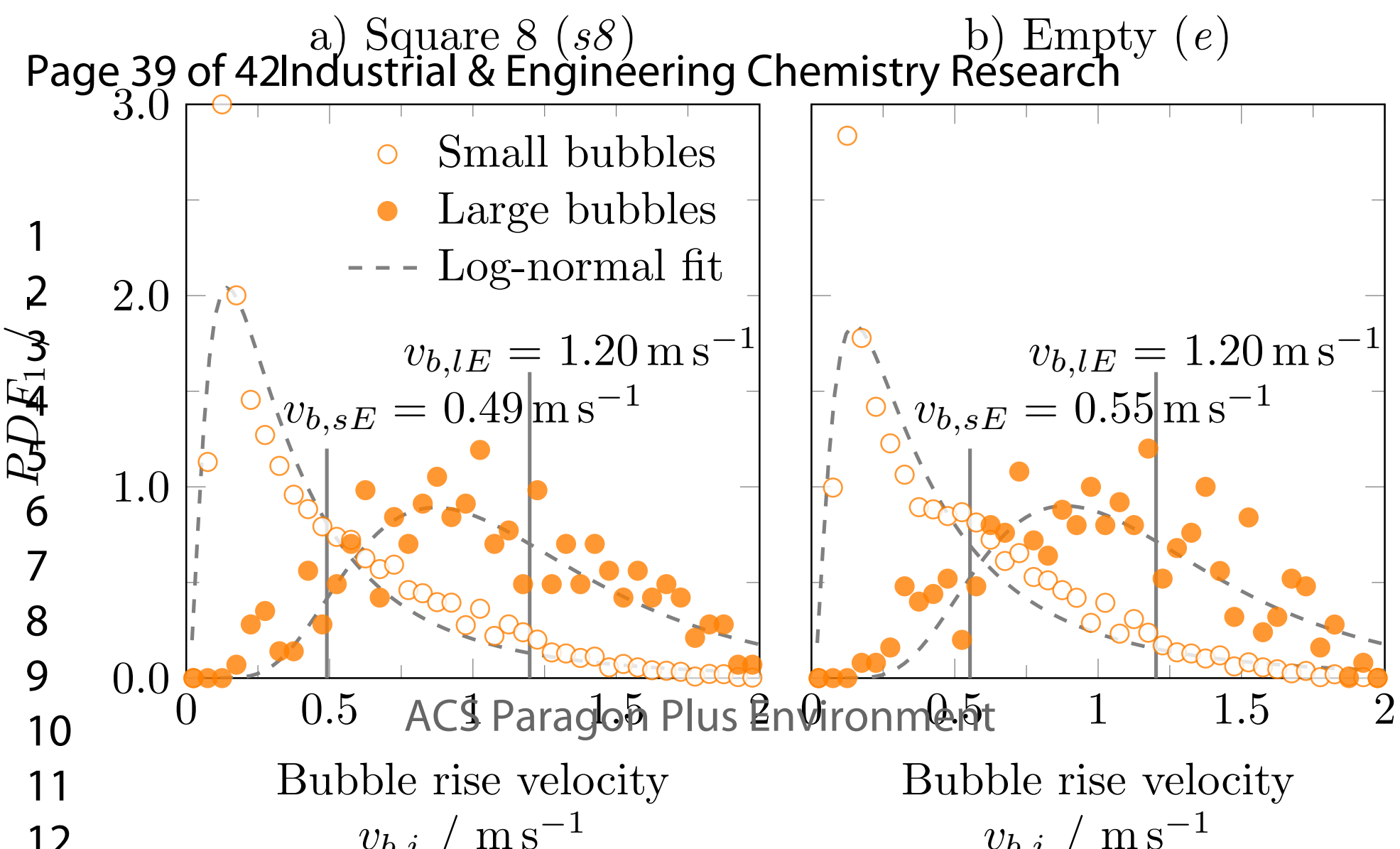

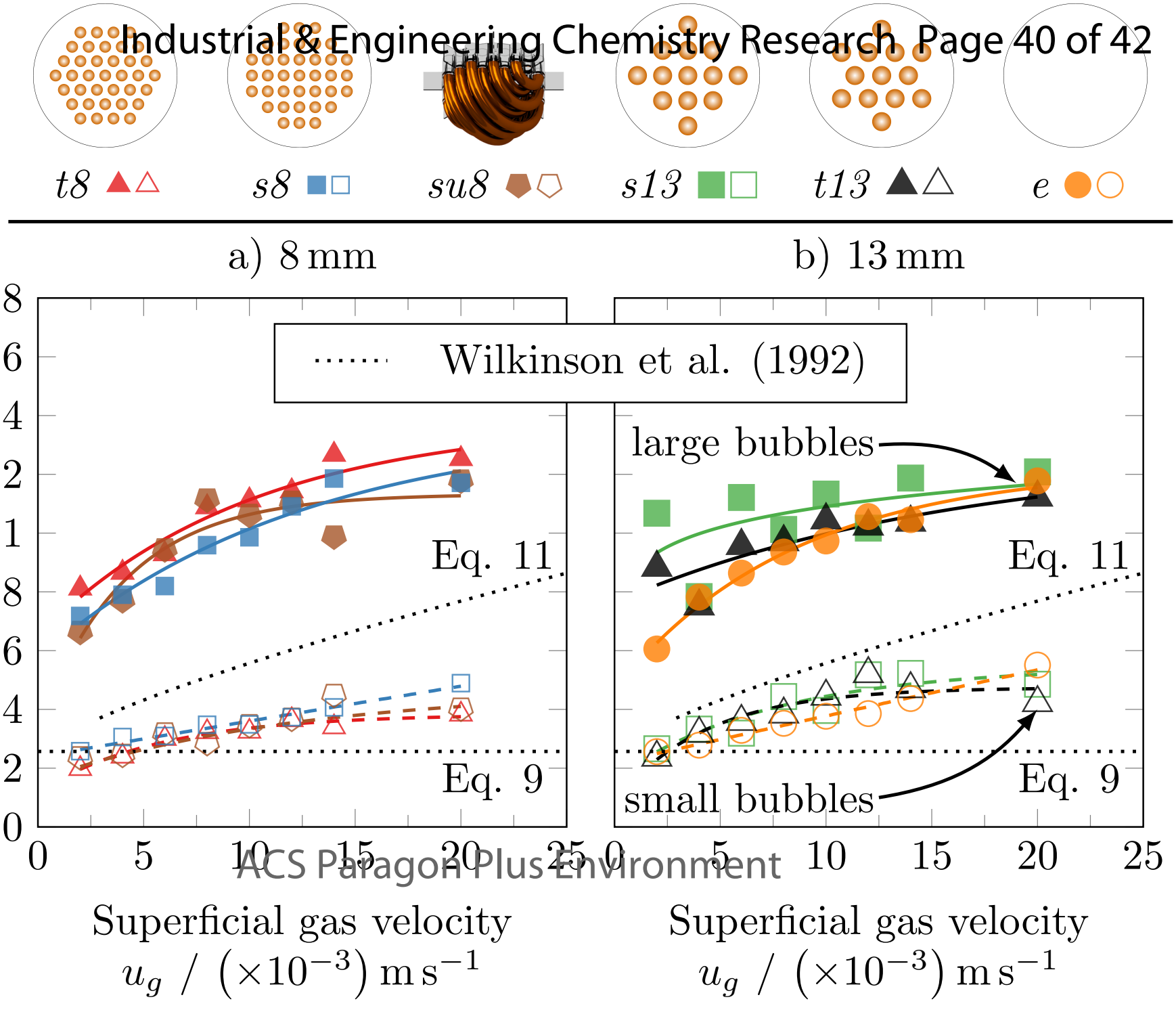

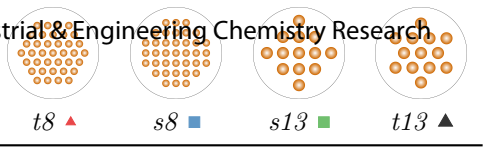

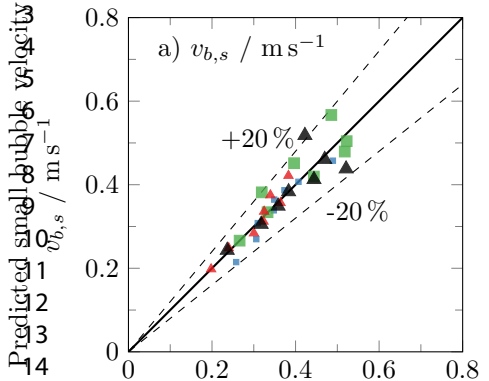

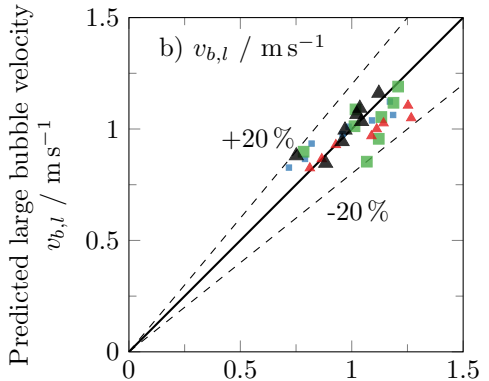

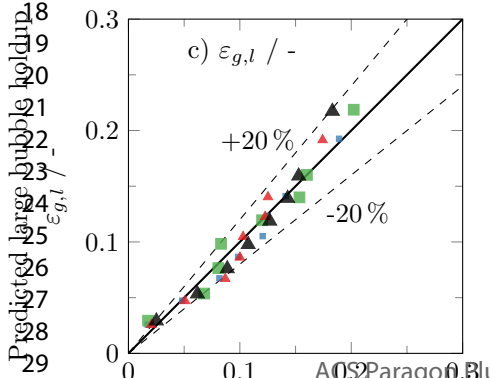

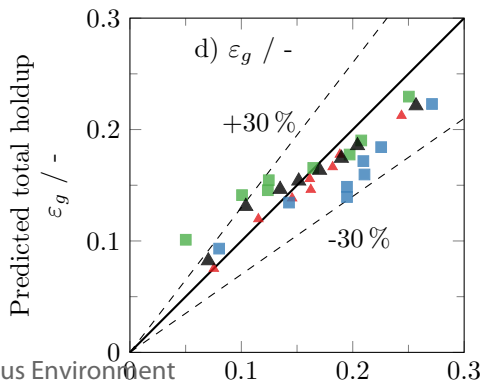

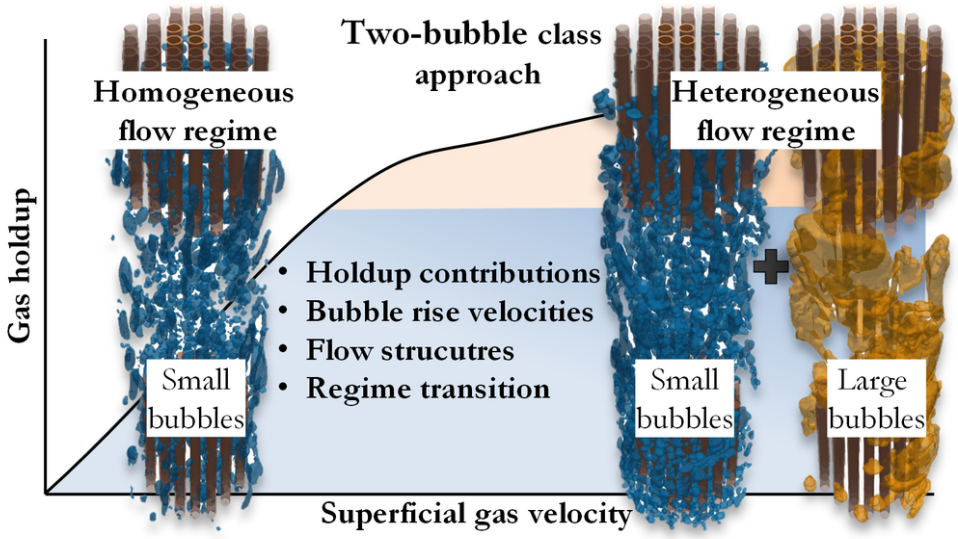

Graphical abstract

87x50mm (300 x 300 DPI)